DIPLOMARBEIT

Modelling of UV disinfection reactors by means of Computational Fluid Dynamics

ausgeführt am
Atominstitut der österreichischen Universitäten
TU Wien
unter der Anleitung von
Univ. Prof. Dr. Norbert Vana

durch
Christoph BUCHNER
Im Park 6
3382 Loosdorf

Wien, 14. November 2006

Christoph Buchner

Kurzzusammenfassung

Heutzutage wird Wasserdesinfektion mit ultravioletter (UV) Strahlung immer wichtiger. Diese Arbeit stellt eine Simulationsmethode zur Vorhersage der Desinfektionwirksamkeit einer UV Desinfektionsanlage vor und vergleicht die Ergebnisse mit biodosimetrischen Messungen.

Berechnungen mit numerischer Strömungssimulation (CFD) wurden für einen Satz von Betriebsparametern durchgeführt. Ein diskretes Phasenmodell wurde verwendet, um Partikelbewegung zu berechnen. Die Fluenzratenverteilung im Reaktor wurde mit verschiedenen Strahlungsmodellen simuliert. Die Partikelbahnen und Strahlungsverteilungen wurden kombiniert, um die Reduktionsäquivalente Fluenz (REF), eine wichtige Größe in der Biodosimetrie, zu berechnen. Die errechneten Simulationsergebnisse werden mit experimentellen Daten verglichen um die erreichte Genauigkeit zu beurteilen.

Der simulierte Druckverlust des Reaktors stimmt sehr gut mit den Experimenten überein. Im Gegensatz zu den biodosimetrischen Messungen werden nur wenig Daten über das Strömungsfeld und die Fluenzratenverteilung von österreichischen Normgutachten erfasst. In Anbetracht dessen wurden von der vorgestellen Simulationsmethode gute Vorhersagen der REF erreicht. Der durchschnittliche Fehler schwankt, abhängig vom verwendeten Strahlungsmodell, zwischen 7 und 25%. Simulationen mit leicht veränderter Geometrie wurden durchgeführt und Fluenzhistogramme wurden berechnet, womit die Vorteile der Simulation gegenüber klassischer biodosimetrischer Analyse verdeutlicht wurden. Der mögliche Einsatz dieser Methode, um UV Desinfektionsanlagen zu entwickeln und zu verbessern wurde sehr gut veranschaulicht.

Abstract

Nowadays, water disinfection with ultraviolet (UV) radiation becomes increasingly important. This work presents a simulation method to predict the disinfection efficacy of an UV disinfection reactor and compares the results to biodosimetric measurements.

Computational Fluid Dynamics (CFD) calculations have been performed for a set of operation parameters. A discrete phase model was used to generate particle tracks. The fluence rate distribution inside the reactor has been simulated using several radiation models. Particle tracks and radiation distributions have been combined to calculate the reduction equivalent fluence (REF), an important quantity in biodosimetry. The obtained simulation results are compared to experimental data to assess the achieved accuracy.

The simulated pressure loss of the reactor agreed very well with the experiments. In contrast to the biodosimetric measurements, only a limited amount of data for the flow field and fluence rate distribution is provided by Austrian standard certification procedures. Considering this, good predictions of the REF were obtained by the presented simulation method. Average error values varies between 7 and 25%, depending on the chosen radiation model. Simulations have been done for a slightly different geometry, and fluence histograms have been calculated, showing the advantages of simulation over classical biodosimetric analysis. The potential use of this method for designing and improving UV disinfection reactors has been demonstrated very well.

Acknowledgements

I am deeply grateful for the valuable support and guidance of my company mentor at arsenal research, Christoph Reichl, and my faculty mentor Norbert Vana.

Furthermore, I would like to thank all the members of the CFD group at arsenal research for answering all the questions that turned up in the course of writing this thesis. I would also like to acknowledge Georg Hirschmann at arsenal research for providing the experimental data on the examined UV disinfection reactor and his help in interpreting them. Regina Sommer and Alexander Cabaj are gratefully acknowledged for valuable discussions and the provided scientific input.

At last, I would like to thank my family and friends for providing their much appreciated support while I was working on this thesis.

Contents

Introduction

Disinfection of potable and wastewater using additives like chlorine, ozone or silver has a long tradition [1]. However, these treatments can result in the formation of disinfection by-products which are harmful to humans. Additionally, certain microorganisms are particularly resistant to chemical disinfection.
Treatment with UV radiation offers a way out, since it does not involve chemicals, producing very few by-products compared to chemical methods, while not altering taste or chemical composition of the water. For this reason, water treatment with ultraviolet radiation becomes increasingly important.

The efficacy of UV disinfection reactors strongly depends on several design and operation parameters. This is why great care has to be exercised when adjusting these parameters to achieve optimal operation. In a normal design process, one of the last stages is the certification of the reactor for a certain set of operational parameters. In Austria, this certification uses biodosimetric tests (frequently called "bioassay") according to ÖNORM M 5873-1 [2]. If this certification fails, the design process has to be repeated. The certification procedure and necessary construction of a prototype is costly and time-consuming.

The increasingly powerful numerical simulation techniques available enable the designer to predict reactor performance under certain operating conditions without incurring the high cost of prototype construction and certification. This also makes it possible to examine many different parameter configurations with respect to their performance. In the traditional

design process, every examined configuration needs to be certified to determine the disinfection efficacy.

UV disinfection and the associated processes have been investigated by several researchers. The main areas of research are radiation modeling and measurement [3–8], analysis and simulation of the performance of UV disinfection reactors [9–13], bacterial inactivation and repair processes [14–19] and others [20–23]. The guidance manual of the U.S. Environmental Protection Agency [24] provides extensive information on many aspects of the implementation of UV disinfection systems.

The aim of the work at hand is to develop a workflow for predicting the performance of a specific UV disinfection reactor using several simulation techniques. Furthermore, the achieved results are compared with data from several certification procedures for this reactor to decide if the achieved accuracy is sufficient for including the developed procedure into the design process of UV disinfection reactors.

Among the tools used, Computational Fluid Dynamics (CFD) simulates the flow of water and the movement of micro organisms through the reactor. This is coupled with the numerical calculation of the radiation field of the UV-emitting lamp to obtain information about the reduction of microorganisms passing through the reactor.

This work was carried out at the Numerical Flow Simulation group of the Transport Technologies business unit of arsenal research in Vienna, under the supervision of Dr. Christoph Reichl.

1. Methods and Implementation

In this chapter the methods and models which were used to compute UV reactor performance are presented.
Section 1.1 gives an overview of the UV disinfection method and the underlying DNA inactivation process.
In section 1.2, the CFD method is briefly explained and the models and parameters which were used are presented.
Section 1.3 treats the used particle tracking method, while section 1.4 presents the relevant physical quantities of the radiation and the implemented radiation models.
Section 1.5 concludes chapter 1 by presenting the computational routines used to merge the previously computed data and distill the relevant information from them.

1.1. UV water disinfection

The first application of ultraviolet light for water disinfection happened in the early 1900s. However, increasing concern about disinfection by-products from other disinfection methods (e.g. chlorination) has only speeded up development of UV disinfection (UVD) in the last few decades [23]. A general overview over the method can be found, among others, in [22, 23].

1.1.1. Advantages and disadvantages

The main advantages and disadvantages of UVD are [1, 21, 22]:

+ UVD does not involve chemical additives. The reproductive ability of microorganisms is destroyed by harming their DNA with UV light (see section 1.1.3). Therefore few disinfection by-products are formed which can harm life forms in contact with the water, as opposed to chemical disinfection methods.
+ UVD is effective against most microorganisms, whereas certain types are resistant to chlorination [1].
+ No hazardous chemicals have to be generated, handled or stored on-site.
+ UVD has a shorter contact time compared to other disinfectants.
+ UVD equipment requires less space than other methods.
+ UVD can be used to treat potable water as well as wastewater.
− Operational parameters have to be monitored closely since several factors critically influence disinfection efficacy (E.g. water transmittivity, lamp lifetime, volume flow, flow characteristics).
− Organisms can sometimes repair damaged DNA after disinfection (see section 1.1.4 and [15]).

1.1.2. UV lamps

UV light for disinfection applications is produced in mercury vapor arc lamps. There are two main designs being used:

Low-pressure (LP) lamps use mercury vapor with a pressure of <1.3 kPa. This causes one sharp emission line at a wavelength of 253.7 nm.
Medium-pressure (MP) lamps employ a higher pressure (≈130 kPa). The increased pressure results in increased radiation output, leading to lamps with higher output power compared to LP lamps. Furthermore, the emission spectrum contains wavelengths from far UV (185 nm) to infrared (1367 nm) [15].
See Figure 1.1 for a comparison of spectra for typical LP and MP UV lamps.

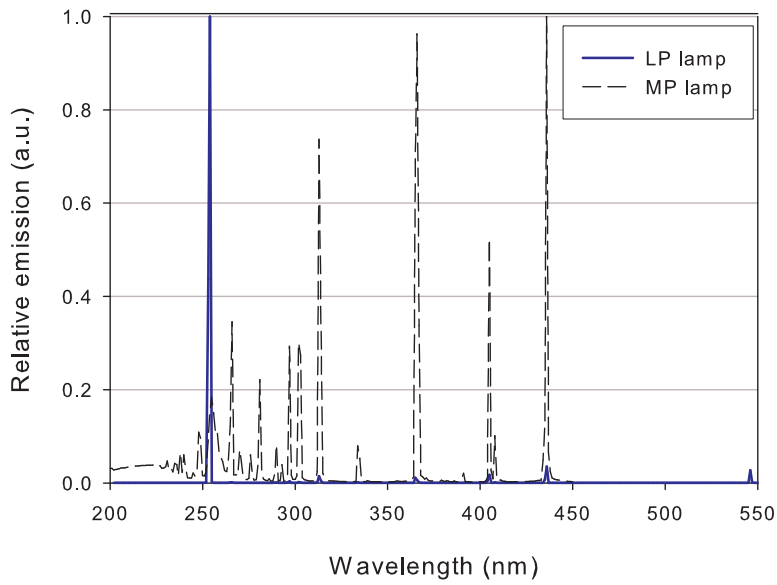

Figure 1.1.: Emission spectra for a typical low-pressure and medium-pressure lamp: *LP:* OSRAM HNS 55W/OFR, *MP:* Heraeus DFH DQ1023 (1 kW), from [25]

1.1.3. The disinfection mechanism

A good explanation of the UV disinfection mechanism is given in [20], which is summarized in the following. See [20] and the references therein for more details.

UV radiation is electromagnetic radiation with a wavelength located in the region between visible light and X-rays. The wavelength range between approximately 100 and 380-400 nm is divided into three bands: UV-C (100-200 nm), UV-B (200-320 nm) and UV-A (320-400 nm), although the limits of these bands vary slightly in the literature [26–29]. UV radiation is commonly classified as non-ionising radiation, although high-energy UV radiation is able to ionise certain materials. The UV-C band marks the transition from non-ionising to ionising electromagnetic radiation. UV radiation is also created through a different process than x-ray and gamma radiation, which are adjacent to the UV band on the low-wavelength side.

The band between 200 and 300 nm is often called the germicidal region because UV light in this region is lethal to microorganisms. The lethal effect of UV light stems from its destructive impact on desoxyribonucleic acid (DNA).

The absorption spectrum of DNA has a maximum around 260 nm (Figure 1.2), which is very close to the 253.7 nm emission line of LP lamps. Recently, it has been shown that the spectral sensitivity of different microorganisms may deviate significantly from the sensitivity of DNA [19]. The sensitivity spectrum of *Bacillus subtilis*, which is the relevant challenge microorganism for this work (see section 1.1.5), is shown in Figure 1.2 in comparison to DNA sensitivity. While the overall shape of the curves is comparable, significant deviations are recognizable. Data for another challenge microorganism (*MS2 coliphage*, which is mainly used in the USA), indicates even greater deviation from the DNA curve. It can be seen that the LP emission line is situated very well, near the maximum for both DNA and *Bacillus subtilis*.

When using MP pressure lamps, care has to be taken when selecting a sensitivity or action spectrum for calculating disinfection performance because of their multiline emission spectra.

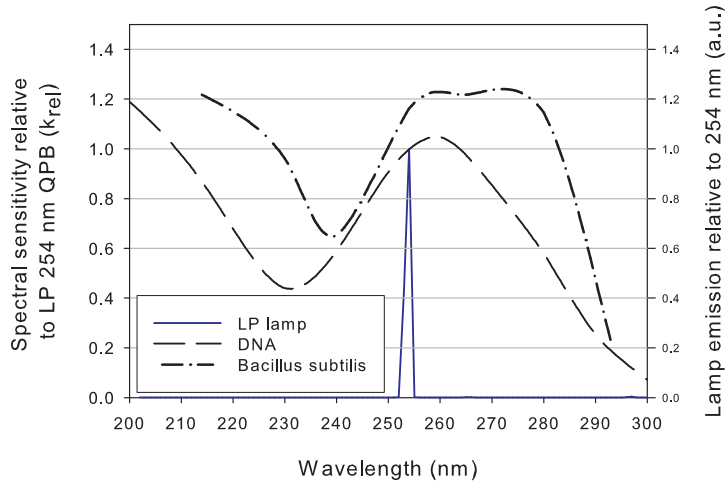

Figure 1.2.: UV sensitivity spectrum of *Bacillus subtilis* spores and DNA, relative to a LP Quasi parallel beam (QPB) experiment, from [19]. Additionally, a LP lamp emission spectrum is shown. It can be seen that the principal LP lamp emission lies in a region of high microorganism sensitivity.

UV light inhibits the reproductive ability of microorganisms by disrupting the replication of DNA as follows:
The DNA components which absorb UV light are the nucleotide bases adenine, guanine, thymine and cytosine. UV absorption of proteins and other cell components is of minor consequence to this process, although it might play a role in the inhibition of DNA repair (see 1.1.4 and [15]).

The following must occur for a photochemical reaction to take place:

1. The radiation must be absorbed by the nucleotide base molecule.

2. The molecule must possess a chemical bond which is of importance to the function of the organism.

3. A sufficient amount of the excitation energy of the absorbed UV photon must reach this vulnerable bond to alter it.

4. After the chemical change the new configuration must endure.

The nucleotides differ in their ability to absorb UV light and undergo a permanent chemical change. The pyrimidines (thymine and cytosine) are ten times more sensitive than the purines (adenine and guanine). Thymine is most susceptible to stable chemical changes. UV light reacts with two adjacent thymine molecules, forming new bonds to produce a thymine double molecule, a *dimer*. This mechanism, which is the most common form of photochemical damage, prevents the replication of the affected microorganism and ultimately results in cell death.

1.1.4. DNA repair

Many organisms have developed mechanisms to compensate for the damage inflicted by UV radiation. Two major pathways have evolved to repair DNA damage, *nucleotide excision repair* and *photoreactivation*. Nucleotide excision repair ("Dark repair") involves more than a dozen proteins that coordinate the removal of DNA damage. Photoreactivation ("Photorepair") uses an enzyme called photolyase to reverse UV-induced damage to DNA. This process is light-dependent, requiring wavelengths from 300 to 500 nm [15, and references therein].

In drinking water distribution systems, water can sometimes take a long time to reach the consumer, giving microorganisms opportunity to carry out dark repair. Furthermore, exposure to light cannot be totally avoided during and after treatment, giving increased significance to photorepair.

It has been found that there are substantial differences between LP and MP irradiation with respect to photorepair. Research might indicate that irradiation with the multiline spectrum of MP lamps damages some component vital to the repair process, thereby suppressing photorepair after MP lamp exposure [15].

1.1.5. Biodosimetry

The last step in the UVD reactor design process is to check if the reactor reaches the necessary disinfection efficacy under specified operating parameters. This certification is realized with the biodosimetry or bioassay method:
A surrogate (challenge) microorganism is injected into the UVD system. The reduction (i.e. the fraction of surviving microorganisms) is measured for a set of desired operating parameters (mainly flow rate, water transmittivity, lamp power) by cultivating and counting samples from before and after flowing through the reactor.

Since the delivered UV fluence[1] cannot be simply measured directly (e.g. with a sensor), the received fluence has to be related to the surrogate microorganism's reduction in a separate test. This relation, the survival curve, is normally generated with a collimated beam experiment beforehand. This curve is now used to determine the so-called reduction equivalent fluence (REF) from the reduction values (see section 1.4.10 for details).

The Austrian standard for UV water disinfection with LP UVD reactors, ÖNORM M 5873-1 [2], requires a minimum REF of $400\,J/m^2$ and *Bacillus subtilis* spores as a challenge microorganism. The spores are roughly cylindrical with approximately $1\,\mu m$ in length and $0.5\,\mu m$ in diameter (Figure 1.3). A detailed description of certification processes can be found in [24].

Recently, the actual fluence distribution of a reactor has been measured using fluorescent microspheres instead of microorganisms. This technique could improve confidence in the use of mathematical models for UVD and complement biodosimetric testing [3].

This work compares biodosimetric results from available certification reports [30–32] to the data obtained with CFD simulation.

[1] See section 1.4.1 for detailed information on radiation nomenclature

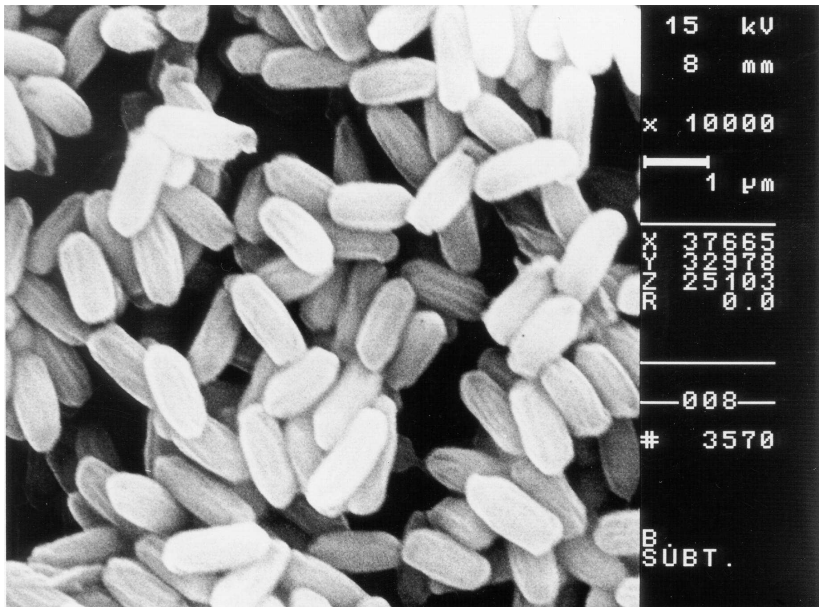

Figure 1.3.: Electron microscope picture of *Bacillus subtilis* spores, from [33]

1.2. Computational Fluid Dynamics

Computational Fluid Dynamics (CFD) *is the science of predicting fluid flow, heat transfer, mass transfer (as in perspiration or dissolution), phase change (as in freezing or boiling), chemical reaction (e.g. combustion), mechanical movement (e.g. fan rotation), stress or deformation of related solid structures (such as a mast bending in the wind), and related phenomena by solving the mathematical equations that govern these processes using a numerical algorithm on a computer [34].*

In this work, CFD was used to obtain the flow field of the water and the motion of particles in the UVD reactor.

1.2.1. Fluid dynamics

The governing equations for fluid flow are the *mass conservation equation* or *continuity equation* (1.1) and the *momentum conservation equation* (1.2), here in the formulation for a fixed control volume in a Cartesian grid [35]:

$$\frac{\partial \rho}{\partial t} + \frac{\partial(\rho u_j)}{\partial x_j} = 0, \tag{1.1}$$

$$\frac{\partial(\rho u_i)}{\partial t} + \frac{\partial(\rho u_i u_j)}{\partial x_j} = \sum f_i, \tag{1.2}$$

where ρ is the density, x_i (i=1,2,3) or (x,y,z) are the Cartesian coordinates, u_i are the Cartesian components of the velocity vector $\boldsymbol{v}$, and f_i are the Cartesian components of the forces acting on the control volume. These forces consist of body forces (gravity, centrifugal and Coriolis forces, electromagnetic forces, etc.) and surface forces (pressure, normal and shear stresses, surface tension, etc.). If not given in index notation, vectors are written in ***bold***, while tensor quantities are set in sans-serif throughout this work.

For Newtonian fluids (like water), the stress tensor T can be written as

$$\mathsf{T}_{ij} = -\left(p + \frac{2}{3}\mu\frac{\partial u_j}{\partial x_j}\right)\delta_{ij} + 2\mu\mathsf{D}_{ij}, \tag{1.3}$$

where D_{ij} is the rate of strain (deformation) tensor

$$\mathsf{D}_{ij} = \frac{1}{2}\left(\frac{\partial u_i}{\partial x_j} + \frac{\partial u_j}{\partial x_i}\right). \tag{1.4}$$

p is the pressure and μ is the dynamic viscosity of the fluid, while δ_{ij} is the Kronecker symbol. The viscous part of the stress tensor is often described as

$$\tau_{ij} = 2\mu\mathsf{D}_{ij} - \frac{2}{3}\mu\delta_{ij}\frac{\partial u_k}{\partial x_k}. \tag{1.5}$$

Equation (1.2) is now written as

$$\frac{\partial(\rho u_i)}{\partial t} + \frac{\partial(\rho u_i u_j)}{\partial x_j} = \frac{\partial \mathsf{T}_{ij}}{\partial x_j} + \rho b_i, \tag{1.6}$$

which is obtained by applying Gauss' divergence theorem to an integral formulation of Eq. (1.2). b_i are the cartesian components of the body forces. Using Eq. (1.5), the momentum conservation equation can be expressed as

$$\frac{\partial(\rho u_i)}{\partial t} + \frac{\partial(\rho u_i u_j)}{\partial x_j} = \frac{\partial \tau_{ij}}{\partial x_j} - \frac{\partial p}{\partial x_i} + \rho g_i. \tag{1.7}$$

The only body force considered here stems from the gravitational acceleration g_i.

For the flow situation at hand, the flow can be assumed to be *incompressible* (constant density) and *isothermal* (constant viscosity). This is because the working fluid is water, whose compressibility can be neglected [35], and the heat transfer from the lamp to the water was deemed negligible due to the insulating air layer between the lamp and the quartz sleeve (see section 1.2.2 for a detailed description of the UVD reactor).

These assumptions reduce Eq. (1.1) to

$$\frac{\partial(\rho u_j)}{\partial x_j} = 0. \tag{1.8}$$

Inserting Eq. (1.5) into Eq. (1.7) yields

$$\rho\frac{\partial u_i}{\partial t} + \rho\frac{\partial(u_i u_j)}{\partial x_j} = \mu\frac{\partial}{\partial x_j}\left(\frac{\partial u_i}{\partial x_j} + \frac{\partial u_j}{\partial x_i}\right) - \frac{2}{3}\mu\delta_{ij}\frac{\partial^2 u_k}{\partial x_j \partial x_k} - \frac{\partial p}{\partial x_i} + \rho g_i. \tag{1.9}$$

Using equation (1.8) twice, (1.9) becomes

$$\frac{\partial u_i}{\partial t} + \frac{\partial(u_i u_j)}{\partial x_j} = \nu\frac{\partial^2 u_i}{\partial x_j \partial x_j} - \frac{1}{\rho}\frac{\partial p}{\partial x_i} + g_i, \tag{1.10}$$

where $\nu = \mu/\rho$ is the kinematic viscosity.

Employing these equations, the fluid flow can be calculated. Unfortunately, even the smallest turbulent processes have to be considered, demanding an extremely high mesh resolution. This simulation approach is called direct numerical simulation (DNS), and is nowadays mostly used in very small scientific applications. For industrial CFD, the computational demand is simply too high. Thus, these small turbulent processes have to be modeled to reduce the computational effort. To this end, many turbulence models have been developed. See section 1.2.4 for details concerning turbulence models.

1.2.2. The UVD reactor

Water disinfection happens in reactor vessels. Water containing living pathogens flows into the reactor where it is exposed to UV radiation, receiving a certain amount of radiation. After leaving the reactor, a sufficient amount of the pathogens has to be inactive for the disinfection process to be effective.

There are two basic designs: Open-channel and closed-channel systems. They are primarily used for wastewater and drinking (potable) water applications, respectively.

In open channel systems, racks with UV lamps are submerged in water flowing through an open channel. The water level in such a channel has to be monitored closely, because if too much water flows over the racks, with lowered exposure to UV light, disinfection performance deteriorates rapidly.

In closed channel systems, water under pressure flows through a closed reactor vessel which contains UV lamps. A known problem here is short-circuiting of the reactor, i.e. water flowing along an unforeseen short path with minimal UV exposure.

Typically, LP and MP lamps are used in both designs. The lamps can be arranged parallel or perpendicular to the flow direction.

The reactor which is the subject of this work is a stainless steel single-LP-lamp, closed-channel reactor designed for flow rates ranging from 0.7 to $6\,m^3/h$, with lamp power ratings of $60\,W$ [30], $80\,W$ [31] and $130\,W$ [32] (Figure 1.4). It has been certified by *ÖFPZ Arsenal Ges.m.b.H.*. The exact titles of the certification reports are not given in the references because of confidentiality reasons.

As a first step, the reactor geometry was modeled with *SolidWorks 2005*. As can be seen in Figure 1.5, the model comprised not only the reactor vessel itself, but also an inlet region (a) before the inlet pressure sensor (b), an elbow connected to the reactor vessel and an outlet pipe (d). It was important to include these segments into the actual simulation, because they mimicked the situation at certification as closely as possible, and they had a great influence on the velocity distribution of the flow entering the reactor.

The reactor vessel had an inner diameter of $100\,mm$ and a length along the main axis of $1048\,mm$. The quartz sleeve protecting the UV lamp was located along the main axis of the reactor and had an outer diameter of $30\,mm$ and a wall thickness of $2\,mm$, running along the entire length of the reactor. The inlet and outlet pipes had several different diameters ranging

Figure 1.4.: Photograph of the reactor ready for certification

from 37 to 43 mm, creating several forward and backward facing steps in those regions. Shortly above the reactor vessel inlet, an annular turbulator plate with 8 evenly spaced circular holes (e) was welded into the reactor.

Some features of the real reactor were not modeled because they would have unnecessarily complicated the mesh while having very little impact on the water flow. Among those were two small ventilation valves near the top and bottom of the reactor vessel, the welding seams of the vessel, and the roughness of the inlet and outlet pipe walls. Furthermore, the exact geometry at the sensor window (c) had to be simplified to permit meshing, and the pressure sensor (which features holes in the wall connected to a manifold, thereby averaging pressure along the circumference of the pipe) has not been modeled at all, instead averaging pressure over a plane at the sensors' location with the CFD software.

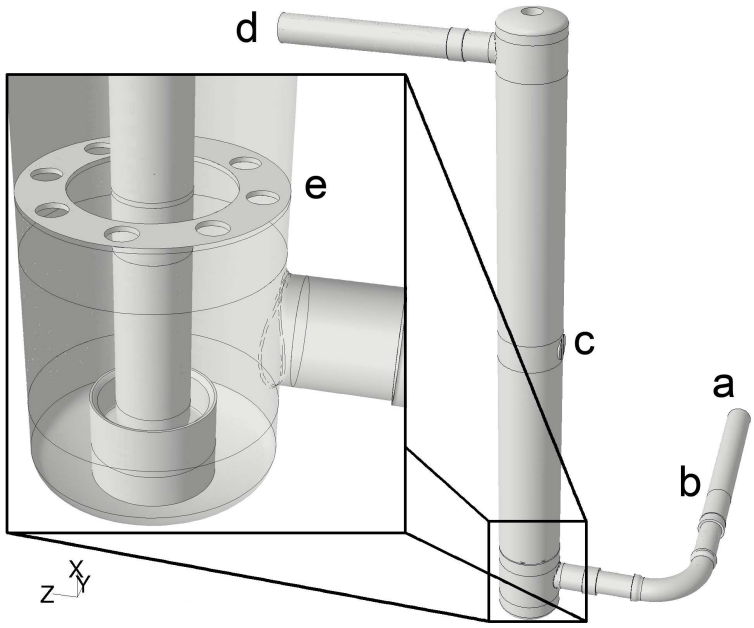

Figure 1.5.: 3D model of the UVD reactor: *a*: water inlet, *b*: pressure sensor, *c*: UV sensor window, *d*: water outlet. The inset shows an enlarged, semitransparent view including the turbulator plate (*e*).

1.2.3. Meshing

CFD generally needs the flow domain to be divided into a grid or mesh. This is essentially a discrete representation of the domain with a number of small volumes, which permits the relevant equations to be solved numerically [35]. Grid construction typically requires a significant part of the project time and much experience of the engineer when working on an industry project.

The geometry from *SolidWorks* was imported into *Gambit 2.2.30*, a meshing software by *Fluent, Inc.*, which was used to construct a mesh. Due to the topology of the problem, a combination of structured and unstructured mesh regions had to be chosen.

The grid resolution for the UVD reactor was chosen such that the smallest detail important for the water flow was sufficiently resolved. For the examined reactor, the smallest features were the holes in the aforementioned annular turbulator plate (see Fig. 1.5, inset). The circumference of these holes was divided into 20 elements (Figure 1.6a). The basic element size was determined as $1.2\,mm$. This size was used when meshing the quartz sleeve surface, the region where the flow enters and exits the main reactor vessel, the steps in the inlet and outlet pipes and other flow-critical sections. For the rest of the geometry, the mesh was gradually coarsened wherever possible to minimize the total number of cells and with it computational demand.

The cell count of the resulting mesh was approximately 3 million cells, which rose to approximately 3.17 million cells when an adaptation of wall regions was performed in *Fluent*. The surface mesh of the outlet region can be seen in Figure 1.6b. A grid adaptation, which divided cells to improve resolution, can be clearly recognized in both Figures 1.6a and 1.6b, e.g. where the outlet pipe meets the reactor vessel.

Gambit provides the user with several mesh quality parameters. The two parameters mainly employed for the mesh at hand were *EquiAngle Skew* and *EquiSize Skew* [36, section 3.4.2].

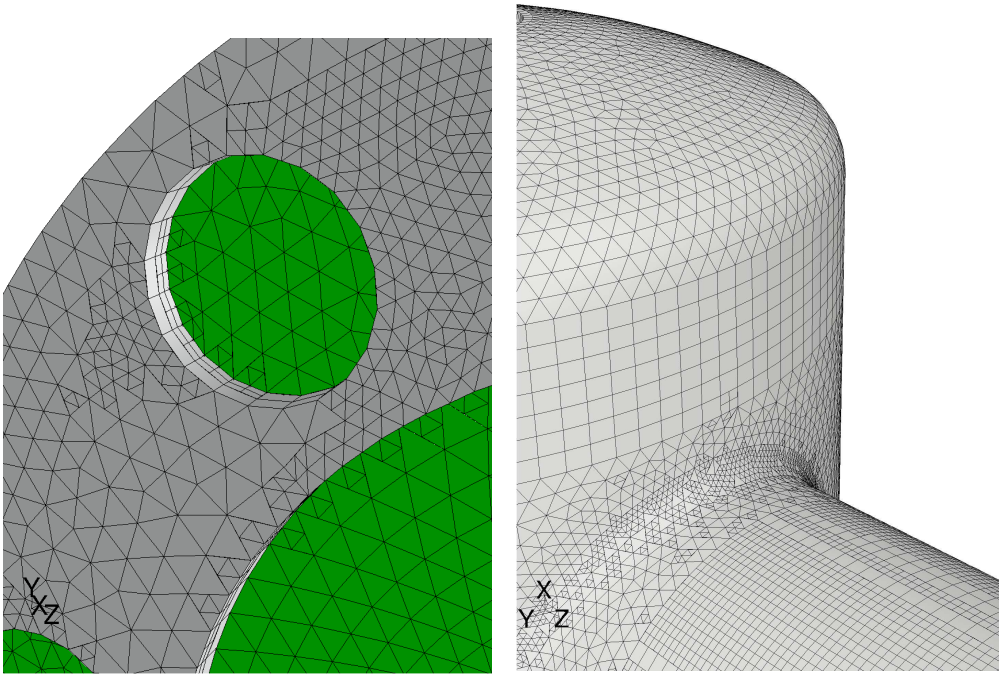

(a) Mesh at the annular turbulator plate (b) Surface mesh in the inlet region

Figure 1.6.: Mesh examples

EquiAngle Skew measures the deviation of a 2D or 3D cell's angles from an equilateral cell. This means an equilateral cell has an EquiAngle Skew of 0, while a degenerate cell has an EquiAngle Skew of 1.

EquiSize Skew is a similar parameter, judging the deviation of the surface and volume of 2D and 3D cells, respectively, from the value for an equilateral cell with the same circumscribing radius. Again, values for the EquiSize Skew vary between 0 and 1, where a low value is desirable.

A maximum Equisize Skew of 0.75 and a maximum EquiAngle Skew of 0.81 could be obtained for the mesh, where the worst cells were located in regions meshed with tetrahedra due to the complex geometry.

1.2.4. CFD calculation

The CFD software used in this work was the commercial package *FLUENT*, Version 6.2.16, on the 30-PC computing cluster of arsenal research. Each computer features a $3\,GHz$ CPU, $3\,GB$ RAM and $1000\,MBit$ Ethernet.

Boundary conditions

For the whole UVD system, only two boundary regions were necessary. At the inlet, a *mass flow inlet* boundary condition was chosen as appropriate. The mass flow was easily adjusted and calculated from the volume flow given in the certification reports [30–32]. A *pressure outlet* was deemed appropriate at the end of the outlet pipe to represent water flowing out of the pipe. Thus, the pressure loss in the reactor, an important performance parameter, could easily be determined. Values for density and viscosity of water at the pressure and temperature given by the certification reports have been obtained online from a NIST database [37].

Concerning fluid dynamics, the most important variable parameter was the volume flow rate. In the certification reports, the volume flow rate varied from 0.691 to $6.047\,m^3/h$, with two groups around $3.5\,m^3/h$ respectively $6\,m^3/h$, and the rest below $2.5\,m^3/h$.

A detailed overview over the different operational cases that were simulated is given in Table 1.1. Here, the parameters relevant for UVD have been given, but others have been omitted to preserve clarity:
Case denotes the case designation: The first number signifies to which certification report the data belongs: "1" [30], "2" [31] and "3" [32]. The following letter specifies the first ("A") or second ("B") run of the measurement. The following number varies with volume flow, and an asterisk denotes if the desired reference irradiance at the sensor has been reached with (constant) full lamp power, but reduced UV transmittivity (no asterisk) or with full transmittivity and reduced lamp power (asterisk).
$\dot{V}$ *(*m^3/h*)* is the volume flow rate.
T_{100} is the transmittivity of a $100\,mm$ thick layer of water for light with a wavelength of $253.7\,nm$.
E_r *(*W/m^2*)* is the reference irradiance value as obtained from the UV reference sensor mounted in the reactor.
Δp *(*Pa*)* is the pressure loss for the whole system, from the inlet pressure sensor to the outlet.
REF (W/m^2*)* is the reduction equivalent fluence as explained in section 1.4.10.

A plot of volume flow rate vs. pressure loss can be found in Figure 2.1 in the results section on page 61, where a quadratic behavior can be observed.

Turbulence modeling

Turbulent flows are characterized by fluctuating velocity fields. These fluctuations mix transported quantities such as momentum, energy, and species concentration, and cause the transported quantities to fluctuate as well. Since these fluctuations can be of small scale and high frequency, they are too computationally expensive to simulate directly in practical engineering calculations. Instead, the instantaneous (exact) governing equations can be time-averaged, ensemble-averaged, or otherwise manipulated to remove the small scales, resulting in a modified set of equations that are computationally

Table 1.1.: Validation measurement data, from [30–32]

Case	$\dot{V}$ (m^3/h)	T_{100}	$E_r(W/m^2)$	$\Delta p(Pa)$	$REF(J/m^2)$
1A1	2.4010	0.36	33.00	342	574
1A2	1.8200	0.21	25.50	205	571
1A2*	1.8370	0.85	24.80	206	539
1A1*	2.4110	0.85	33.80	346	540
1B1	2.5310	0.40	34.00	381	509
1B2	1.8090	0.21	26.00	204	546
1B2*	1.7890	0.86	25.80	209	581
1B1*	2.4100	0.85	33.10	345	541
2A1	3.5400	0.40	51.00	677	600
2A2	2.0970	0.21	39.80	345	742
2A2*	2.1010	0.87	38.70	340	639
2A1*	3.5040	0.86	50.70	656	540
2B1	3.4960	0.40	51.00	668	632
2B2	2.1150	0.22	39.50	335	818
2B2*	2.1000	0.87	39.30	332	814
2B1*	3.5030	0.86	51.00	668	630
3A1	6.047	0.37	64.5	1938	424
3A2	3.500	0.19	48.0	650	520
3A2*	3.506	0.82	47.8	652	548
3B1	5.974	0.35	61.3	1899	404
3B2	3.502	0.20	46.0	656	537
3B2*	3.517	0.84	48.2	672	520
3B1*	5.974	0.84	62.1	1898	400

less expensive to solve. However, the modified equations contain additional unknown variables, and turbulence models are needed to determine these variables in terms of known quantities [34].

The Reynolds number, based on the reactor's inlet pipe diameter and the area-averaged inlet flow velocity varies between approximately 14000 and 46000 for the given operational parameters (refer to section 1.2.4 for details). Therefore, the flow is in the turbulent regime, making turbulence modeling necessary.

The **realizable k-ϵ turbulence model** ($rk\epsilon$) is an improved k-ϵ model, and as such belonging to the class of 2-equation Reynolds-averaged Navier-Stokes (RANS) models. Two separate transport equations are formulated for the turbulent kinetic energy k (Equation 1.11) and the dissipation rate ϵ (Equation 1.12) to achieve closure of the system of equations. In our case, certain terms (e.g. for buoyancy and compressibility) can be neglected, yielding

$$\frac{\partial(\rho k)}{\partial t} + \frac{\partial(\rho k u_j)}{\partial x_j} = \frac{\partial}{\partial x_j}\left[\left(\mu + \frac{\mu_t}{\sigma_k}\right)\frac{\partial k}{\partial x_j}\right] + G_k - \rho\epsilon \tag{1.11}$$

$$\frac{\partial(\rho \epsilon)}{\partial t} + \frac{\partial(\rho \epsilon u_j)}{\partial x_j} = \frac{\partial}{\partial x_j}\left[\left(\mu + \frac{\mu_t}{\sigma_\epsilon}\right)\frac{\partial \epsilon}{\partial x_j}\right] + \rho C_1 S\epsilon - \rho C_2 \frac{\epsilon^2}{k + \sqrt{\nu\epsilon}}, \tag{1.12}$$

$$\text{where } C_1 = \max\left[0.43, \frac{\eta}{\eta + 5}\right], \quad \eta = S\frac{k}{\epsilon}, \quad S = \sqrt{2S_{ij}S_{ij}}$$

Here, G_k represents the production of turbulent kinetic energy, μ_t is the turbulent viscosity defined by $\mu_t = \rho C_\mu \frac{k^2}{\epsilon}$, σ_k and σ_ϵ are the turbulent Prandtl numbers for k and ϵ, respectively, and S_{ij} is the mean rate-of-strain tensor. The model constants have been established as $C_2 = 1.9$, $\sigma_k = 1.0$, $\sigma_\epsilon = 1.2$ by several commonly known experiments published elsewhere.

In contrast to other k-ϵ models, C_μ in the turbulent viscosity expression is variable in the realizable k-ϵ model. In combination with the modified ϵ transport equation (1.12), this ensures that the model satisfies certain mathematical constraints on the normal stresses, consistent with the physics of turbulent flows.

This model was chosen because it is most suitable for the flow situation at hand of all available 1- and 2-equation models [34]. It has been extensively validated for a wide range of flows, including rotating homogeneous shear flows, free flows including jets and mixing layers, channel and boundary layer flows, and separated flows. For all these cases, the performance of the model has been found to be substantially better than that of the standard k-ϵ model. Especially noteworthy is the fact that the realizable k-ϵ model resolves the round-jet anomaly; i.e., it predicts the spreading rate for axisymmetric jets as well as that for planar jets [34].

While the bulk of CFD simulation has been performed with the realizable k-ϵ model, four cases have additionally been simulated with the **Detached Eddy Simulation (DES)** model. The small number of computations stems from the fact that the computational effort is several orders of magnitude larger for DES compared to $rk\epsilon$. A steady $rk\epsilon$ case simulation was typically finished overnight, while an unsteady DES simulation, even for very short time periods, typically took weeks to finish.

In the DES model, a Large Eddy Simulation (LES) model is combined with a RANS model. In the core region of the flow, where large turbulent structures play a dominant role, the LES model is used, while near walls, the RANS model takes over. In *Fluent*, the one-equation Spalart-Allmaras model is used for the RANS part. In the LES model, turbulence is calculated for large structures down to a certain threshold size, below which modeling is used. The rationale behind this is that by modeling less of turbulence (and resolving more), the error introduced by turbulence modeling can be reduced. It is also believed to be easier to find a "universal" model for the small scales, since they tend to be more isotropic and less affected by the macroscopic features like boundary conditions, than the large eddies [34].

LES and DES are normally too computationally demanding for engineering applications. Consequently, RANS models are mostly used.

Wall treatment

Turbulent flows are significantly affected by the presence of walls. Obviously, the mean velocity field is affected through the no-slip condition that has to be satisfied at the wall. However, the turbulence is also changed by the presence of the wall in non-trivial ways. Very close to the wall, viscous damping reduces the tangential velocity fluctuations, while kinematic blocking reduces the normal fluctuations. Toward the outer part of the near-wall region, however, the turbulence is rapidly augmented by the production of turbulence kinetic energy due to the large gradients in mean velocity.

The near-wall modeling significantly impacts the fidelity of numerical solutions, inasmuch as walls are the main source of mean vorticity and turbulence. After all, it is in the near-wall region that the solution variables have large gradients, and the momentum and other scalar transports occur most vigorously. Therefore, accurate representation of the flow in the near-wall region determines successful predictions of wall-bounded turbulent flows [34].

Traditionally, there are two approaches to modeling the near-wall region:

In one approach, the viscosity-affected inner region (viscous sublayer and buffer layer) is not resolved. Instead, semi-empirical formulas called "wall functions" are used to bridge the viscosity-affected region between the wall and the fully-turbulent region. The use of wall functions obviates the need to modify the turbulence models to account for the presence of the wall.

In another approach, the turbulence models are modified to enable the viscosity-affected region to be resolved with a very fine mesh all the way to the wall, including the viscous sublayer ("near-wall modeling").

Cell size requirements dictated by the reactor geometry precluded the use of wall functions. Thus, in this work, a model combining said two approaches has been used, the "Enhanced Wall Treatment" [34].

The computation mesh has been adapted such that cell size requirements for the Enhanced Wall Treatment were fulfilled as well as possible in the reactor volume. This was accomplished by following guidelines [34] con-

cerning the nondimensional wall distance $y^+ = \frac{\rho u_\tau y}{\mu}$. Here, $u_\tau = \sqrt{\tau_w \rho}$ is the friction velocity, y the distance to the wall and τ_w the wall shear stress.

1.3. Particles

The challenge microorganism used in the certification reports was the spore of *Bacillus subtilis* ATCC *(American Type Culture Collection)* 6633 in a concentration of approximately 10^7 spores per liter water. The spores are roughly cylindrical with an approximate length of $\mathbf{1}\,\boldsymbol{\mu m}$ and a width of $\mathbf{0.5}\,\boldsymbol{\mu m}$ [33]. This results in a volume fraction of the spores in the water of $\approx 2 \cdot 10^{-9}$.

Biodosimetry measures the reduction of bacteria as they pass through the UVD system, and relates this reduction to a REF. The shortcoming of this approach is that only one value for reactor efficacy is obtained, and identification of bad disinfection regions in the reactor is very difficult.

Recently, research has been going on which tries to take biodosimetry one step further: By using fluorescent microspheres instead of microorganisms, not only the mean fluence, but also a fluence distribution can be obtained [3].

CFD simulation is the next step with regard to the amount of extractable information. With this method, individual particle tracks are calculated by using adequate particle tracking models. Even individual particles which received a low fluence can be identified and their paths in the reactor plotted, thereby facilitating identification of problematic regions in the reactor.

1.3.1. Equations of motion for particles

To obtain particle paths from the CFD solution, the particle modeling capabilities of *Fluent* were used. *Fluent* offers a Lagrangian particle model with stochastic tracking (random walk) capabilities which is described in the following sections as in [34]:

A particle is tracked by integrating the force balance on the particle in a Lagrangian reference frame. This force balance equates the particle inertia with the forces acting on the particle, and can be written as

$$\frac{d\boldsymbol{u}_p}{dt} = \underbrace{F_D(\boldsymbol{u} - \boldsymbol{u}_p)}_{\text{drag}} + \underbrace{\frac{\boldsymbol{g}(\rho_p - \rho)}{\rho_p}}_{\text{buoyancy}} + \underbrace{\boldsymbol{a}_o}_{\text{others}}. \tag{1.13}$$

Here, $\boldsymbol{u}_p$ is the particle velocity, $\boldsymbol{u}$ the velocity of the carrier fluid (water), $F_D(\boldsymbol{u} - \boldsymbol{u_p})$ the drag force per unit particle mass, $\boldsymbol{g}$ the gravitational acceleration, ρ_p and ρ the particle and carrier fluid density, respectively, and $\boldsymbol{a}_o$ other accelerations (e.g. due to magnetic fields).
Since the spore density is approximately the density of the carrier fluid, the buoyancy term can be neglected. Furthermore, there are no other forces involved in the problem, which reduces the force balance to

$$\frac{d\boldsymbol{u}_p}{dt} = F_D(\boldsymbol{u} - \boldsymbol{u}_p) \tag{1.14}$$

$$F_D = \frac{18\mu}{\rho_p d_p^2}\frac{C_D \mathrm{Re}_r}{24} \tag{1.15}$$

Re_r is the relative Reynolds number, defined as

$$\mathrm{Re}_r \equiv \frac{\rho d_p |\boldsymbol{u}_p - \boldsymbol{u}|}{\mu}, \tag{1.16}$$

where μ is the dynamic viscosity, d_p the particle diameter and C_D the nonspherical drag coefficient

$$C_D = \frac{24}{Re_{sph}}(1 + b_1 Re_{sph}^{b_2}) + \frac{b_3 Re_{sph}}{b_4 + Re_{sph},} \tag{1.17}$$

where

$$
\begin{aligned}
b_1 &= \exp(2.3288 - 6.4581\Phi + 2.4486\Phi^2) \\
b_2 &= 0.0964 + 0.5565\Phi \\
b_3 &= \exp(4.905 - 13.8944\Phi + 18.4222\Phi^2 - 10.2599\Phi^3) \\
b_4 &= \exp(1.4681 + 12.2584\Phi - 20.7322\Phi^2 + 15.8855\Phi^3)
\end{aligned} \tag{1.18}
$$

The shape factor Φ is defined as $\Phi = \frac{s}{S}$, where s is the surface area of a sphere having the same volume as the particle, and S is the actual surface of the particle. The Reynolds number Re_{sph} is computed with the diameter d_{sph} of a sphere having the same volume.

For the cylindrical spores of *Bacillus subtilis* with a length of $1\,\mu m$ and a diameter of $0.5\,\mu m$, $\boldsymbol{\Phi = 0.832}$ and $\boldsymbol{d_{sph} = 0.721\,\mu m}$.

This formulation represents the appropriate one of several options available for the drag term for cylindrical particles of the given size.

1.3.2. Stochastic tracking

In the stochastic tracking approach, *Fluent* predicts the turbulent dispersion of particles by integrating the trajectory equations for individual particles, using the instantaneous fluid velocity, $\boldsymbol{u} = \bar{\boldsymbol{u}} + \boldsymbol{u}'$, along the particle path during the integration of (1.14). $\bar{\boldsymbol{u}}$ is the mean velocity and $\boldsymbol{u}'$ is the velocity fluctuation, denoted as usual in fluid dynamics.

Using this approach, the random effects of turbulence on the particle motion may be accounted for. Thus, it is possible to calculate multiple particle trajectories with a common point of origin, all of which are different. The number of calculated trajectories per point of origin is an important parameter of the simulation. It will be called the *"number of tries"* in this work. By increasing the number of tries, it is possible to obtain as many particle paths as needed for a reliable statistical examination. In Figure 1.7, the paths of three "tries" for a single particle are shown.

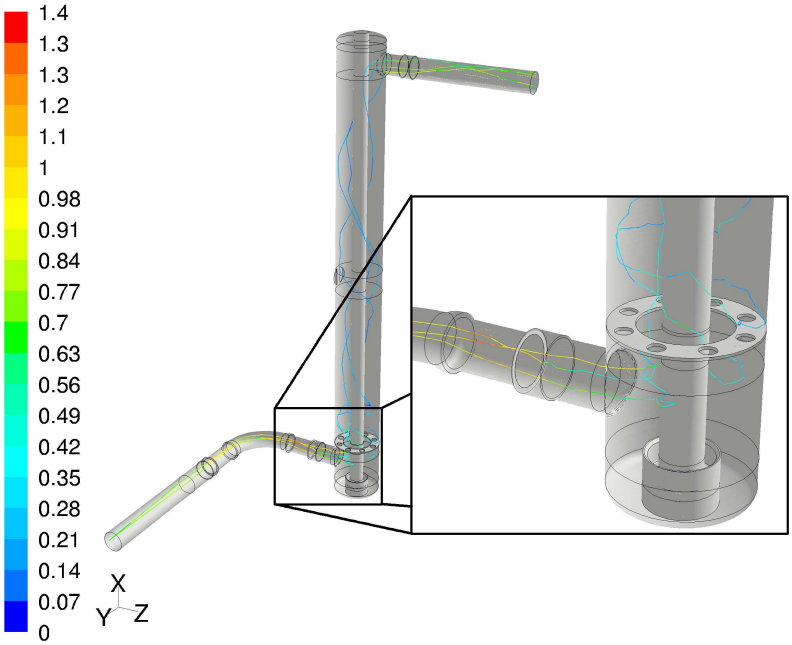

Figure 1.7.: Paths of three tries for a single particle. The impact of random effects leads to non-identical paths. The inset shows an enlarged view of the lower portion of the reactor vessel. Paths colored by particle velocity magnitude (m/s).

Discrete Random Walk model

In the Discrete Random Walk *(DRW)* model, or "eddy lifetime" model, the interaction of a particle with a succession of discrete stylized fluid phase turbulent eddies is simulated. Each eddy is characterized by a Gaussian distributed random velocity fluctuation, u', v', and w' (the 3 cartesian components of $\boldsymbol{u}'$), and a time scale, τ_e.

The values of u', v', and w', which remain constant over τ_e, are sampled by assuming that they obey a Gaussian probability distribution, so that $u' = \zeta\sqrt{\overline{u'^2}}$, where ζ is a normally distributed random number, and the remainder of the right-hand side is the local RMS value of the velocity fluctuations. Since the kinetic energy of turbulence is known from the CFD calculation at each point in the flow, these values of the RMS fluctuating components can be defined (assuming isotropy) as $\sqrt{\overline{u'^2}} = \sqrt{\overline{v'^2}} = \sqrt{\overline{w'^2}} = \sqrt{2k/3}$.

The particle is assumed to interact with the eddy over the time scale τ_e. This time scale is either the eddy lifetime or the time it takes the particle to cross the eddy, whichever is smaller. After this time is reached, new values for u', v', and w' are being calculated.

Thus, information about the turbulence, which is obtained from the CFD model, is included into the particle motion equations.

Using this particle tracking model, it has been assumed that the particle motion does not influence the water flow in the reactor. Thus, coupling of the water and particle motion is unnecessary. Furthermore, particle concentration has to be so low that particle-particle interaction is negligible. Keeping in mind the small size ($1\,\mu m$ diameter) and low volume fraction of the particles ($V_p/V_{fluid} = 2 \cdot 10^{-9}$), these assumptions are justified.

The particle data is output as a *.fvp* file containing position and time data for every particle, for every "try". A routine has been written to bring these data into a format better suitable for the subsequent UVD simulation. Data processing routines are described in detail in section 1.5.

1.4. Radiation

1.4.1. Basics

In the following, an overview of some radiation-related definitions and principles is given to clarify and assist in the understanding of this work. This overview has been adapted from Bolton [8].

- **Source radiant power** (Φ): the radiant power (W) emitted in all directions by a radiant energy source.

- **Irradiance** (E): the total radiant power from all directions *incident* on an infinitesimal element of *surface* area dS containing the point under consideration, divided by dS. The SI unit of irradiance is W/m^2. For a position of distance r from a point source in a non-absorbing medium, the irradiance is given by $E = \frac{\Phi}{4\pi r^2}$.

- **Fluence rate** (E'): the radiant power passing from all directions *through* an infinitesimally small *sphere* of cross-sectional area dA, divided by dA. The SI unit of fluence rate is W/m^2. Note that *fluence rate* and *irradiance* are similar, but conceptually quite different terms. Since a microorganism can receive UV radiation from any direction (especially with multiple lamps involved), fluence rate is the appropriate term to use in a UV reactor.

- **Fluence or UV Dose** (H'): defined as the total radiant energy from all directions passing through an infinitesimally small sphere of cross-sectional area dA, divided by dA. The fluence is the *fluence rate* times the irradiation time in seconds. The SI unit of fluence is J/m^2.

- **Refraction and Snell's Law**: Snell's Law governs the refraction properties of radiant energy transmitted through an interface between two media,

$$n_1 \sin\theta_1 = n_2 \sin\theta_2, \tag{1.19}$$

where n_1 and n_2 are the refractive indices of the two media, and θ_1 and θ_2 the angles of the incident respectively refracted beam to a line perpendicular to the interface.

- **Reflection and the Fresnel Law**: Whenever radiant energy passes through an interface between two media of different refractive indices, a certain fraction of the radiant energy is reflected at the angle $\theta_r = \theta_1$, the rest passes through the interface into the second medium and undergoes refraction. The optics involving the description of this process are complicated, since the amount reflected depends on the polarization of the radiant energy. If $r_\perp$ is the amplitude of radiant energy *perpendicular* to the plane of incidence and $r_\parallel$ is the amplitude of the radiant energy *parallel* to the plane of incidence, then the Fresnel Laws define these two amplitudes as

$$r_\perp = \frac{n_1 \cos\theta_1 - n_2 \cos\theta_2}{n_1 \cos\theta_1 + n_2 \cos\theta_2} \tag{1.20}$$

$$r_\parallel = \frac{n_2 \cos\theta_1 - n_1 \cos\theta_2}{n_2 \cos\theta_1 + n_1 \cos\theta_2} \tag{1.21}$$

  The *Reflectance* R for unpolarized radiant energy is given by

$$R = \frac{1}{2}\left[r_\parallel^2 + r_\perp^2\right]. \tag{1.22}$$

  The *Transmittance* T refracted into the second medium is given by $T = 1 - R$.

- **Absorption**: Water and quartz glass absorb radiation as it travels through these media. The relevant quantity for this absorption, which depends on the distance covered in the respective medium, is the transmittance, with the distance this transmittance is measured for in the subscript. T_{10} for the transmittance value for a $10\,mm$ thick layer and T_{100} for a $100\,mm$ thick layer are commonly used expressions. This transmittance value must not be mixed up with the transmittance value resulting from the reflection/refraction at a me-

dia interface. The distance-dependent transmittance normally also depends on the radiation wavelength. In this work, when not otherwise stated, transmittance values for a wavelength of $254\,nm$ will be used.

The transmittance value for a layer of thickness l (in mm) can easily be calculated as

$$T_l = T_{10}^{\frac{l}{10}}. \tag{1.23}$$

1.4.2. Optics in the reactor

In UVD reactors, UV radiation from the lamp has to travel through a layer of air surrounding the lamp and pass the quartz sleeve encasing the lamp before it reaches the water to be disinfected. This causes the radiation to be attenuated by the reflection and absorption processes explained above as it travels along the optical path. A depiction of these different factors and a typical optical path for the examined UVD reactor is shown in Figure 1.8 on page 35.

It has been found [8] that for drinking water applications (with a water transmittance of $T_{10} > 0.7$), the effects of refraction and reflection have to be included to permit an accurate calculation. For wastewater applications, however, the minor error arising from neglecting refraction and reflection can be accounted for with a simple correction.

The optical parameters of the examined reactor at a wavelength of $\lambda = 254\,nm$ are listed in Table 1.2: n_i are the refraction indices and $T_{10,1}$,$T_{10,2}$ and $T_{10,3}$ are the transmittance coefficients for air, quartz and water, respectively. For simplicity, the subscript "10" will be omitted from now on, and the transmittance for $10\,mm$ will be meant if not stated otherwise.

The geometrical parameters of the reactor relevant for radiation calculations are given in Table 1.3. The x-axis is the main axis of the reactor, and the last two given values are the extent of the main reactor vessel in the x direction. The origin of the coordinate system is situated at the intersection between the influent pipe centerline and the x-axis, with positive x in

Table 1.2.: Optical parameters of the examined reactor at a wavelength of $\lambda = 254\,nm$. n_2 from [25], n_3 from [38]

	Air	Quartz	Water
Refractive index	n_1 1	n_2 1.506	n_3 1.376
Transmittance	$T_{10,1}$ 1.0	$T_{10,2}$ 0.8208	$T_{10,3}$ 0.84-0.99

Table 1.3.: Radiation-relevant geometrical parameters of the examined reactor. x-values in relation to coordinate system origin

Thickness of air layer	r_1	$0.013\,m$
Thickness of quartz layer	r_2	$0.002\,m$
Maximum thickness of water layer	$r_{3,max}$	$0.035\,m$
Lamp beginning, x-coord.	x_{LB}	$0.008\,m$
Lamp end, x-coord.	x_{LE}	$0.913\,m$
Reactor beginning, x-coord.	x_{RB}	$-0.075\,m$
Reactor end, x-coord.	x_{RE}	$0.973\,m$

flow direction. Radiation calculations have only been made in a cylindrical volume with radius $r_1 + r_2 + r_3$ and length $x_{RE} - x_{RB}$. This made some significant simplifications in calculation procedures possible, while excluding the influent and effluent pipes from the radiation calculation. Although, due to the high transmittance value of drinking water, a significant amount of radiation can reach the pipes, only a small section of the lamp is visible there, thereby greatly reducing the fluence received by particles while in the pipes.

1.4.3. Calculation procedure

The fluence rate was determined for a cylindrical grid of points in the calculation volume described above, using different radiation models. This grid made it possible to later determine the fluence rate at each particle position by bilinear interpolation. Thus, the computationally expensive fluence rate calculation only had to be performed once for the whole calculation vol-

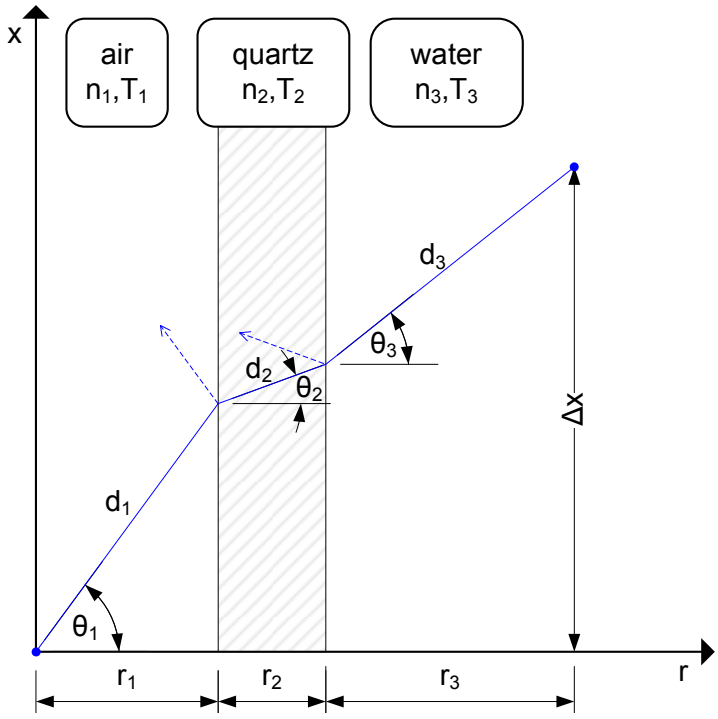

Figure 1.8.: Optical path in the UVD reactor. Light is traveling from a point source at the origin to the destination coordinate.

ume. This approach was much more efficient than calculating the fluence rate separately for every position in each particle path. See section 1.5.2 for more information on the necessary grid resolution.
With the fluence rate known for each particle position and time, the accumulated fluence for each particle could be determined by numerical integration.

Calculation of refraction angles

To be able to calculate the fluence rate at a given point, one has to obtain the refraction angles. Figure 1.8 displays the optical path in the reactor. $\Theta_1, \Theta_2, \Theta_3$ are refraction angles, d_1, d_2, d_3 the optical path lengths and r_1, r_2, r_3 the radial distances for air, quartz and water, respectively.

The three refraction angles are related by Snell's Law (1.24). Another relation can be obtained from simple trigonometry (1.25).

$$n_1 \sin\theta_1 = n_2 \sin\theta_2 = n_3 \sin\theta_3 \tag{1.24}$$

$$r_1 \tan\theta_1 + r_2 \tan\theta_2 + r_3 \tan\theta_3 = \Delta x \tag{1.25}$$

To get a relation which only depends on θ_1, these equations are combined to

$$r_1 \tan\theta_1 + r_2 \tan\left[\arcsin\left(\frac{n_1}{n_2}\sin\theta_1\right)\right] + r_3 \tan\left[\arcsin\left(\frac{n_1}{n_3}\sin\theta_1\right)\right] = \Delta x. \tag{1.26}$$

With $\arcsin x = \arctan\dfrac{x}{\sqrt{1-x^2}}$ this simplifies to

$$r_1 \tan\theta_1 + r_2 \frac{n_1 \sin\theta_1}{\sqrt{n_2^2 - n_1^2 \sin^2\theta_1}} + r_3 \frac{n_1 \sin\theta_1}{\sqrt{n_3^2 - n_1^2 \sin^2\theta_1}} = \Delta x \tag{1.27}$$

$$r_1 \tan\theta_1 + n_1 \sin\theta_1 \left[\frac{r_2}{\sqrt{n_2^2 - n_1^2 \sin^2\theta_1}} + \frac{r_3}{\sqrt{n_3^2 - n_1^2 \sin^2\theta_1}}\right] = \Delta x \tag{1.28}$$

Unfortunately, this equation can only be solved numerically. For the details of the numerical solution please see section 1.5.2.

Once θ_1 has been found, all other variables can easily be calculated, and the fluence rate for the coordinates in question can be obtained.

The focus effect

Another component of refraction is the focus effect [9]. Considering no refraction, the radiation power emitted from a point source within a finite difference angle $2\Delta\theta_1$ (see Figure 1.9) and traveling for a distance of $d_1 + d_2 + d_3$, would cover a circle with a diameter of g_{WO}.

When using cylindrical symmetry, this cross-section becomes a frustum or truncated cone of area A_{WO} with an aperture angle of $2\theta_1$, the lamp axis as frustum axis and the generatrix g_{WO} (in red in Fig. 1.9).

Now, when including refraction at the media interfaces while keeping the optical path length $d_1 + d_2 + d_3$ constant, this frustum has the area A_W, the aperture angle $2\theta_3$ and the generatrix g_W (in blue). Liu [9] introduced the so-called *focus factor*, which describes the extent by which the focus effect concentrates the light, thus changing the fluence rate at any given point. This focus factor is the ratio of the two aforementioned frustum areas:

$$Focus = \frac{A_{WO}}{A_W} \tag{1.29}$$

Considering small angles $\Delta\theta$ for the whole following calculations allows significant simplifications. The area A_{WO} can be obtained from the general formula $A_{WO} = (R + r)\pi m$, where R and r are the bigger respectively smaller radii of the frustum, and m is the length of the generatrix g_{WO}. Inserting the relevant variables for our case, this becomes

$$A_{WO} = 2(d_1 + d_2 + d_3)\cos\theta_1 \cdot \pi \cdot 2\Delta\theta_1(d_1 + d_2 + d_3) \tag{1.30}$$

$$A_{WO} = 4\pi(d_1 + d_2 + d_3)^2 \cos\theta_1 \Delta\theta_1 \tag{1.31}$$

Calculating A_W, the same approach is used:

$$g_W = (h'' - h')\cos\theta_3 \tag{1.32}$$

$$A_W = 2(r_1 + r_2 + r_3) \cdot \pi \cdot \cos\theta_3(h'' - h') \tag{1.33}$$

$$h'' = r_1 \tan(\theta_1 + \Delta\theta_1) + r_2 \tan(\theta_2 + \Delta\theta_2) + r_3 \tan(\theta_3 + \Delta\theta_3) \tag{1.34}$$

$$h' = r_1 \tan(\theta_1 - \Delta\theta_1) + r_2 \tan(\theta_2 - \Delta\theta_2) + r_3 \tan(\theta_3 - \Delta\theta_3) \tag{1.35}$$

All angles $\Delta\theta$ can be calculated from $\Delta\theta_1$ with Snell's law (1.19). Using trigonometric function relations and exploiting $\Delta\theta_1 \ll 1$, $h'' - h'$ becomes

$$h'' - h' = r_1 \frac{4\Delta\theta_1}{1 + \cos(2\theta_1)} + r_2 \frac{4\Delta\theta_2}{1 + \cos(2\theta_2)} + r_3 \frac{4\Delta\theta_3}{1 + \cos(2\theta_3)} \tag{1.36}$$

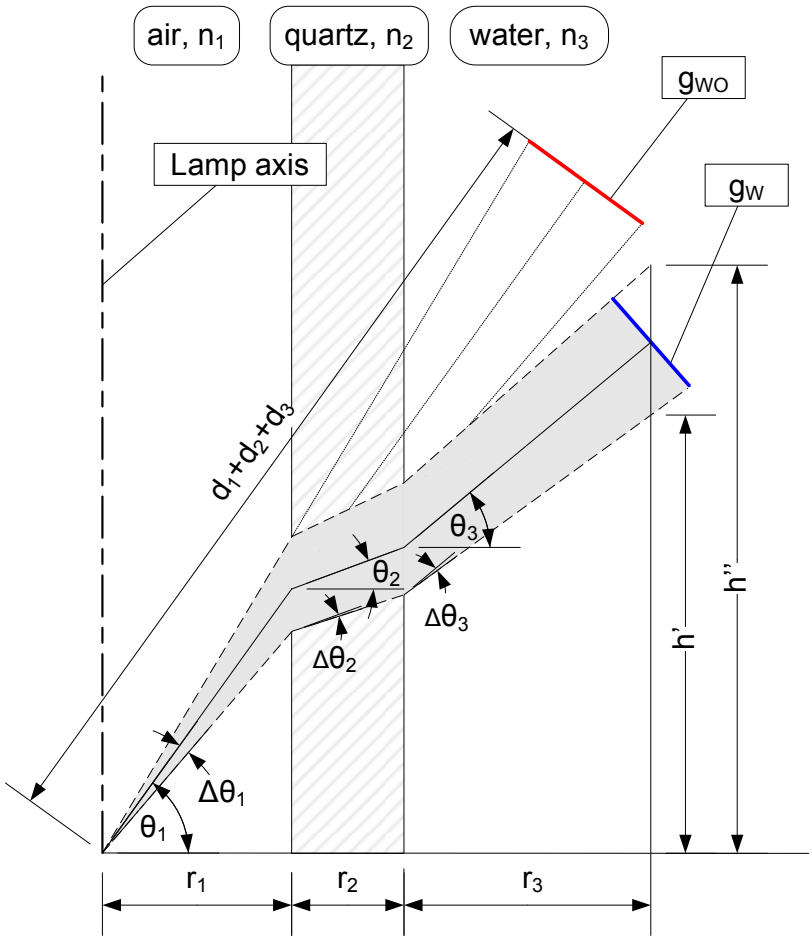

Figure 1.9.: The focus effect: The optical path with and without refraction and the resulting generatrices g_W and g_{WO} for the focus effect calculation are shown.

To ease calculation, all angles $\Delta\theta$ are related to $\Delta\theta_1$, which finally yields

$$h'' - h' = 2\Delta\theta_1 \cos\theta_1 n_1 \left(\frac{r_1}{n_1 \cos^3\theta_1} + \frac{r_2}{n_2 \cos^3\theta_2} + \frac{r_3}{n_3 \cos^3\theta_3} \right) \tag{1.37}$$

Combining (1.29),(1.31),(1.33) and (1.37), the focus effect becomes

$$Focus = \frac{(d_1 + d_2 + d_3)^2}{(r_1 + r_2 + r_3)\cos\theta_3 n_1} \left(\frac{r_1}{n_1 \cos^3\theta_1} + \frac{r_2}{n_2 \cos^3\theta_2} + \frac{r_3}{n_3 \cos^3\theta_3} \right) \tag{1.38}$$

One can see that $\Delta\theta_1$ was cancelled out. This means that (1.38) remains unchanged at the limit of $\Delta\theta_1 \to 0$.

In the following sections, the different implemented radiation models and the relevant equations for the determination of the UV reference sensor reading will be described in detail. The routines and algorithms used for the radiation calculation will be explained in section 1.5.

1.4.4. Multiple Point Source Summation (MPSS)

The Multiple Point Source Summation model approximates the emission of a linear lamp by assuming it is equivalent to that of N point sources spaced equally along the lamp. The power output of each point source is Φ/N, where Φ is the total UV power output of the lamp in the wavelength band of interest [8]. Section 1.5.2 explains how the necessary number of sources was determined. The fluence rate at one point of interest is the sum of the fluence rate contributions of all point sources. Since the location of the point sources are different, the path lengths, reflectances and attenuation factors vary with the source index n:

$$E' = \sum_{n=1}^{N} \left(\underbrace{\frac{\Phi/N}{4\pi(d_1 + d_2 + d_3)^2}}_{\text{point source}} \underbrace{(1 - R_{12})(1 - R_{23})}_{\text{reflection at media interfaces}} \underbrace{T_2^{d_2/0.01} T_3^{d_3/0.01}}_{\text{attenuation in media}} \right) \tag{1.39}$$

Here, attenuation effects resulting from reflection at the media interfaces and absorption in quartz and water have already been taken into account according to equations (1.22) and (1.23). R_{12} and R_{23} are the reflectance values for the air-quartz and quartz-water interface, respectively, and d_1, d_2, d_3 are the optical path lengths in air, quartz and water, respectively, as shown in Figure 1.8.

To include the focus effect, (1.39) has to be amended with a term for the focus factor to better represent the physics of the radiation, thus becoming the **MPSS-F** radiation model:

$$E' = \sum_{n=1}^{N} \left(\frac{\Phi/N}{4\pi(d_1 + d_2 + d_3)^2} (1 - R_{12})(1 - R_{23}) T_2^{d_2/0.01} T_3^{d_3/0.01} \mathit{Focus} \right) \tag{1.40}$$

1.4.5. Multiple Segment Source Summation (MSSS)

The MPSS model can be improved by modeling the lamp not as a number of point sources, but as a number of cylindrical segments [5, 9]. This can be achieved by adding a term to the MPSS model (1.39), which decreases with the cosine of the angle between the surface normal of the lamp and the direction vector. Thus, the equation of fluence rate for the **MSSS** model is found as

$$E' = \sum_{n=1}^{N} \left(\frac{\Phi/N}{4\pi(d_1 + d_2 + d_3)^2} (1 - R_{12})(1 - R_{23}) T_2^{d_2/0.01} T_3^{d_3/0.01} \cos\theta_1 \right) \tag{1.41}$$

The MSSS model corrects for an overprediction near the lamp ends and near the lamp surface better than the MPSS model. It can again be amended with the focus factor to create the **MSSS-F** model:

$$E' = \sum_{n=1}^{N} \left(\frac{\Phi/N}{4\pi(d_1 + d_2 + d_3)^2} (1 - R_{12})(1 - R_{23}) T_2^{d_2/0.01} T_3^{d_3/0.01} \cos\theta_1 \mathit{Focus} \right) \tag{1.42}$$

MSSS-F models the physical processes most closely of all models presented in this work, which will be important later on. See section 1.4.8 for details.

1.4.6. Line Source Integration (LSI)

The Line Source Integration model is the continuous or integral version of the MPSS model. These models are mathematically identical as the number of point sources approaches ∞ [9]. However, a computationally fast closed-form solution only exists in absence of absorption, reflection and refraction. To correct for this shortcoming, Liu [9] developed the *attenuation factor approach*, where the LSI model is multiplied with a correcting attenuation factor:

$$I = \frac{P}{4\pi LR}\left[\arctan\left(\frac{L/2+H}{R}\right) + \arctan\left(\frac{L/2-H}{R}\right)\right] \cdot atten \tag{1.43}$$

This yields the fluence rate for a point with the normal distance R from the lamp and a longitudinal distance H from the center of the lamp with length L.

The attenuation factor is obtained by dividing a MPSS, MPSS-F or MSSS-F model with a reduced number of sources N by a simplified N-source MPSS model which only takes into account the point source term, without refraction, reflection, attenuation and focus effect. Section 1.5.2 explains how the number of necessary sources for the LSI models was obtained. An attenuation factor based on MSSS-F was used for the LSI and an attenuation

factor using MPSS was used for the RADLSI model presented in the next section, as recommended in [9].

$$atten_{MSSS-F} = \frac{\sum_{n=1}^{N}\left(\frac{\Phi/N}{4\pi(d_1+d_2+d_3)^2}(1-R_{12})(1-R_{23})T_2^{d_2/0.01}T_3^{d_3/0.01}\cos\theta_1 Focus\right)}{\sum_{n=1}^{N}\left(\frac{\Phi/N}{4\pi(l^2+r^2)}\right)} \tag{1.44}$$

$$atten_{MPSS} = \frac{\sum_{n=1}^{N}\left(\frac{\Phi/N}{4\pi(d_1+d_2+d_3)^2}(1-R_{12})(1-R_{23})T_2^{d_2/0.01}T_3^{d_3/0.01}\right)}{\sum_{n=1}^{N}\left(\frac{\Phi/N}{4\pi(l^2+r^2)}\right)} \tag{1.45}$$

Here, l and r are the longitudinal and radial distances, respectively, from the evaluation point to the particular lamp source. The LSI model using the attenuation factor (1.44) will be used in this study and will be denoted **LSI-F**.

1.4.7. Modified LSI (RADLSI)

It was discovered that the closed-form LSI model predictions become more inaccurate when approaching the quartz sleeve surface. Therefore, a simple correction was developed by Bolton and Liu [9] and called **RADLSI**.

$$I = \min\left\{\frac{P}{2\pi LR}, \frac{P}{4\pi LR}\left[\arctan\left(\frac{L/2+H}{R}\right)+\arctan\left(\frac{L/2-H}{R}\right)\right]\right\}\cdot \cdot atten_{MPSS} \tag{1.46}$$

The first part of the minimum function is a fluence rate calculation based on a radial intensity model, while the second part is the original LSI model.

1.4.8. The reference sensor

An important part of the radiation calculation is the determination of the irradiance of the sensor in the reactor vessel. This is so because this value was the only available radiation measurement with which to check the radiation model. Unfortunately, the conversion efficiency from electrical power to light at 253.7 nm was unknown, and only the electrical power rating was given in [30–32]. Furthermore, some certification cases (as specified in Table 1.1) use reduced lamp power to simulate an aged lamp near the end of its designated lifetime. For these reasons, it was necessary to use a sensor simulation with a MSSS-F model to calibrate our radiation models. The MSSS-F model was deemed most appropriate for this task since it matches the occurring physical processes best of all treated radiation models. The UV conversion efficiency parameter `UV-efficiency_254` was adjusted such that the simulated sensor reading equalled the experimental reading from the certification reports. In this work, `monospaced` letters indicate the name of a configuration file parameter.

The details of the sensor installation are precisely specified in [2]: A 5 mm thick, flat quartz window separates the sensor from the water in the reactor, while a 1 mm thick air gap is located between the sensor surface and said quartz window. The sensor assembly can be recognized in Figure 1.4 on page 15 as the roughly cylindrical structure at middle height of the reactor vessel. Since the sensor is mounted in the wall near the half-point of the reactor vessel axis, pointing to the lamp at a right angle, the radiation field does not vary very much at the sensor location. Therefore, the sensor can be represented by a point and direction in space. For this point, the radiation angle of incidence is calculated, and this information is used to determine the light irradiance which reaches the sensor surface, which is the plane of calibration for the sensor as stated by [2]. Here, irradiance is used instead of fluence rate because the light hits a surface instead of passing through an infinitesimal sphere.

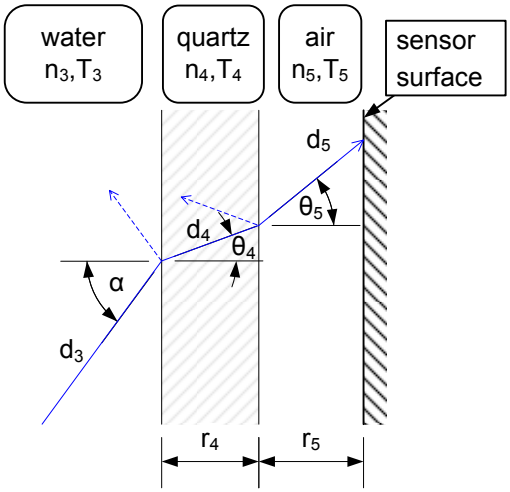

Figure 1.10.: Optical path in the sensor assembly. Light is coming from the lower left.

The path of light entering the sensor assembly (beginning with the window separating the sensor from the reactor vessel) is shown in Figure 1.10. Light passing through the water in the reactor vessel hits the quartz window at an angle of incidence α. Some of it is reflected back, as indicated by the dashed arrow, the rest is refracted at an angle θ_4. Afterwards, the light is reflected and refracted again at the quartz-air-interface, resulting in an incidence angle θ_5 on the sensor surface. When calculating the sensor irradiance value, one has to remember that total reflection can occur at the quartz-air interface. Therefore, the contribution of light with α above a certain threshold has to be discarded. The angle θ_5 is then used to calculate the angle-dependent relative response $\mathfrak{R}_{total}$ of the sensor, as given in [2]:

$$\mathfrak{R}_{total}(\theta) = \cos\theta\, \mathfrak{S}(\theta), \tag{1.47}$$

where $\mathfrak{S}(\theta)$ is the directional sensitivity of the sensor:

$$\begin{aligned} \text{for } 0^\circ \leq \theta \leq 10^\circ: \quad & 0.995 \leq \mathfrak{S} \leq 1, \\ \text{for } 10^\circ < \theta \leq 80^\circ: \quad & \end{aligned} \tag{1.48}$$

$$\begin{aligned} \frac{1.0180942 - 0.011674538\,\theta}{1 - 0.0098891336\,\theta} - 0.00003\,\theta^2 \leq \mathfrak{S} \\ \leq \frac{1.0180942 - 0.011674538\,\theta}{1 - 0.0098891336\,\theta} + 0.00003\,\theta^2 \end{aligned} \tag{1.49}$$

No information concerning $\theta > 80^\circ$ is given in [2]. Since the certification reports [30–32] only state that the sensor fulfills (1.48) and (1.49), the directional sensitivity was set to 1 in the range of (1.48), and the quadratic term was omitted in (1.49), thus yielding the median of the acceptable values for r. Consequently, the relative response of the sensor is:

$$\mathfrak{R}_{total} = \begin{cases} \cos(\theta) & \text{for } 0^\circ \leq \theta \leq 10^\circ \\ \cos(\theta)\dfrac{1.0180942 - 0.011674538\,\theta}{1 - 0.0098891336\,\theta} & \text{for } 10^\circ < \theta \leq 86^\circ \\ 0 & \text{for } \theta > 86^\circ \end{cases} \tag{1.50}$$

Since it is unclear what relationship [2] prescribes for angles bigger than 80°, the upper limit for θ has been expanded to 86° in (1.50), which is located near the root of the used function, to get a continuous relation for $\mathfrak{R}_{total}$.

To calculate the reading of the sensor, an approach corresponding to the used radiation model was used. The expressions for the resultant irradiance for the different models, with added relevant terms from the sensor model, are:

$$\begin{aligned} \text{MPSS: } E = \sum_{n=1}^{N} \Bigg(\mathfrak{R}_{total} \frac{\Phi/N}{4\pi(d_1 + d_2 + d_3 + d_4 + d_5)^2} \cdot \\ \cdot (1 - R_{12})(1 - R_{23})(1 - R_{34})(1 - R_{45}) T_2^{d_2/0.01} T_3^{d_3/0.01} T_4^{d_4/0.01} T_5^{d_5/0.01} \Bigg) \end{aligned} \tag{1.51}$$

$$\text{MSSS: } E = \sum_{n=1}^{N} \left(\mathfrak{R}_{total} \cos\theta_1 \frac{\Phi/N}{4\pi(d_1+d_2+d_3+d_4+d_5)^2} \cdot \right.$$
$$\left. \cdot (1-R_{12})(1-R_{23})(1-R_{34})(1-R_{45}) T_2^{d_2/0.01} T_3^{d_3/0.01} T_4^{d_4/0.01} T_5^{d_5/0.01} \right) \tag{1.52}$$

The T_5 term, although in fact unnecessary for air ($T_{air} = 1$), has been included to facilitate potential modification of the sensor assembly configuration. Models including the focus effect use (1.51) and (1.52), amended with the focus factor.

In the LSI and RADLSI models, the sensor optics and response function only influence the attenuation factor calculation.

1.4.9. Fluence calculation

The fluence received by each particle is the integral over the fluence rate along the particle path. This integral is calculated numerically according to (1.58) and (1.59) in section 1.5.3. After the received fluence has been calculated for each particle, forming the (effluent) fluence distribution, these data are processed to yield the reduction of the challenge microorganism as described in the following section.

1.4.10. Reduction and Reduction Equivalent Fluence

The reduction is the ratio of the number of microorganisms surviving after irradiation (N) to the original number of microorganisms (N_0). It is often given in a decadic logarithm form, $\log_{10}(\frac{N}{N_0})$, then called the log reduction.

The expression relating reduction and received fluence is called survival curve or calibration function. It is unique for each microorganism. For *Bacillus subtilis ATCC 6633*, the challenge microorganism used in the cer-

tification reports [30–32], the survival curve can be described as [2, 16, 17]. The parentheses indicate that $\frac{N}{N_0}$ is a function of H_0:

$$\frac{N}{N_0}(H_0) = 1 - \left(1 - 10^{-kH_0}\right)^{10^d}, \tag{1.53}$$

which is usually plotted in its logarithmic form

$$\log_{10} \frac{N}{N_0}(H_0) = \log_{10} \left[1 - \left(1 - 10^{-kH_0}\right)^{10^d}\right]. \tag{1.54}$$

$k(m^2/J)$ is the slope of the linear part of the survival curve, $H_0(J/m^2)$ is the received fluence and d is the intercept of the linear part with the ordinate. Acceptable ranges of values for k and d are given in [2].

The values found experimentally in [30–32] are shown in Table 1.4. A plot of the survival curves for these values is given in Figure 1.11.

Table 1.4.: Values for the survival curve parameters k and d for different reactor configurations [30–32]

	k	d
[30]	0.0067	0.61
[31]	0.0057	0.60
[32]	0.0057	0.60

To calculate the total reduction of a reactor configuration, one has to evaluate (1.53) for all fluence values occurring in the effluent fluence distribution, normalized with the number of particles [18]. Thus, the total reduction is:

$$\left(\frac{N}{N_0}\right)_{total} = \frac{1}{\mathfrak{N}} \sum_{i=1}^{\mathfrak{N}} \frac{N}{N_0}(H_i), \tag{1.55}$$

where H_i are the fluence values in an effluent fluence distribution of $\mathfrak{N}$ particles.

Now, this reduction is unfortunately specific to the used challenge microorganism, and is therefore not easily comparable to the reduction results of e.g. *Escherichia coli*. To obtain a more comparable quantity, one could

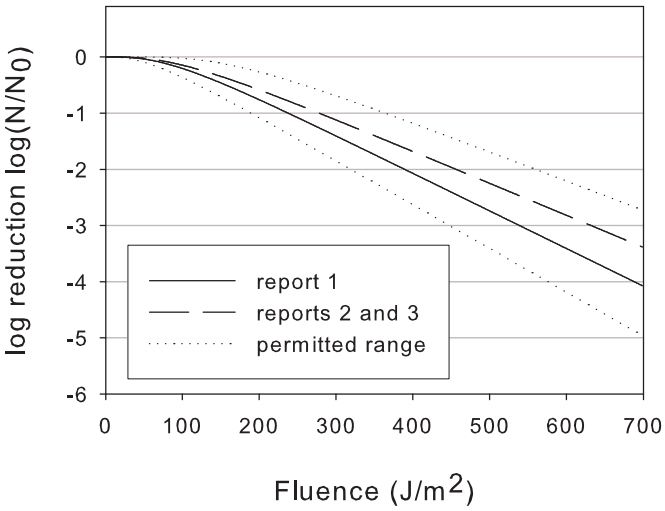

Figure 1.11.: Survival curves of *Bacillus subtilis ATCC 6633* used in [30–32]. The dotted line indicates the permitted range of values for k and d, from [2].

use some kind of mean fluence value. Using just the arithmetic mean of the obtained fluence distribution looks promising at a first glance. Unfortunately, the usage of a biodosimeter with a nonlinear survival curve makes it impossible to get correct results with just the arithmetic mean [17, 18]. Therefore, the fluence distribution has to be weighted with the survival curve, yielding the Reduction Equivalent Fluence *(REF)*. This quantity can easily be calculated by forming the inverse function of the survival curve (1.53),

$$REF = H_0(\frac{N}{N_0}) = -\frac{1}{k}\log_{10}\left[1 - \left(1 - \frac{N}{N_0}\right)^{10^{-d}}\right] \tag{1.56}$$

and inserting the calculated total reduction $(\frac{N}{N_0})_{total}$ [2, 17].

These REF values form the core requirement of the ÖNORM M 5873-1 [2] with regard to disinfection performance: To gain permission for use, a UVD reactor has to (among other things) reach a REF of at least 400 J/m^2.

The reduction and REF play a central role in the assessment of the accuracy of the used CFD, particle, radiation and bacterial models. The obtained results are compared with the data from the certification reports [30–32] in section 2.3.

1.5. Data processing

The UVD simulation was performed using particle tracking data from *Fluent* and a number of routines written on a *Suse Linux* system in the programming language *C*. The produced code amounts for approximately 3000 lines.

In the following sections an overview over the usage of the routines and the algorithms therein is given. The whole code was included into external files (*uv.c* and *uv.h*) to facilitate production of customized processing procedures.

A diagram showing the structure of the simulation process and all files and routines involved can be found in Figure A.1 on page 79 in the appendix.

1.5.1. Particle data

The result of CFD calculations and particle tracking with *Fluent* are saved in *.fvp* files. These files amount for approximately 700 MB per try for the present reactor. To facilitate data processing, a routine was written which converts these data into a custom file format (*.p*xx). This routine contains options to extract the paths of single particles and split large files into smaller portions for parallel processing, if desired. The former option can be useful for identifying regions of bad disinfection performance by enabling the user to plot the path of particles which received a low fluence.

1.5.2. Fluence rate field

After the particle data files have been created, the fluence rate field information has to be calculated.

The central place to define options is a *.cfg* file, which defines all relevant options for the whole calculation. The entries available and their meaning are shown in Table A.1 on page 80 of the appendix.

Data grid

As a first step, a grid with cylindrical symmetry is generated, which encompasses the volume of the reactor vessel, without the influent and effluent pipes, as defined by the `r1-r3`, `reactor_begins_x` and `reactor_ends_x` parameters.

This volume is discretized based on the `cell_size_at_quartz_surface` parameter, which defines the distance of two grid points at the surface of the quartz sleeve. The axial and azimuthal cell sizes are constant, while the radial cell size increases in the outward direction to minimize the number of grid points while maintaining accuracy. This is possible because the curvature of the fluence rate curve in outward direction quickly decreases, thereby enabling fewer grid points to achieve satisfying accuracy for the linear interpolation used.

To be able to analyze several aspects of the fluence rate calculations, several paths and points have been defined at which the fluence rate can be evaluated by using a routine which returns the fluence rate values along a path respectively at a certain point. These paths are depicted in Figure 1.12:

- Path 1 runs axially along the entire length of the reactor, being located at 25% of the distance from the quartz sleeve to the reactor wall ($r = 0.02375\,m$). All paths and points are placed in the arbitrarily chosen plane $z = 0\,m$. Due to the cylindrical symmetry of the fluence rate field, this choice has no influence on the evaluation results.

- Path 2 is the same as path 1, except that it is located at 75% of said distance ($r = 0.04125\,m$).

- Path 3 is a radial path from the quartz sleeve to the reactor wall located at the half-point of the lamp ($x = 0.45\,m$).

- Path 4 is the same as path 3, except that it is located at the upper end of the lamp ($x = 0.913\,m$).

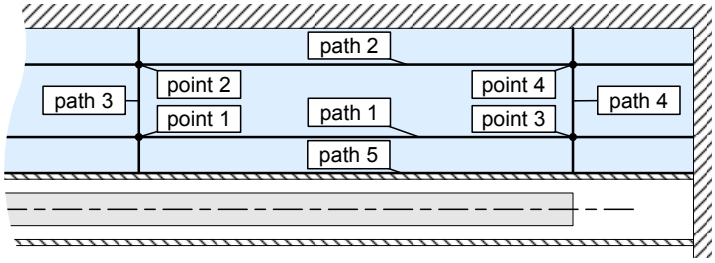

Figure 1.12.: Different evaluation paths and points to analyze the fluence rate field. Figure not to scale.

- The points 1-4 are located at the intersections of all these paths.
- Path 5 is the same as path 1, except that it is located at the surface of the quartz sleeve.

Examining the fluence rate at paths 1-4 for different cell sizes, the value of the `cell_size_at_quartz_surface` parameter necessary for accurate calculations could be determined: At first, the paths were generated with a very high resolution (2100 points for the axial and 100 points for the radial paths). Then, the fluence rate along those paths was calculated for the smallest cell size computationally possible. Memory requirements turned out to limit this cell size to $0.4\,mm$. Thus, a fluence rate was obtained for every point along the respective path. Afterwards, the same calculation was performed for increasing cell size values while calculating the deviation of the fluence rate results for the respective cell size from the fluence rate at $0.4\,mm$. The mean, standard deviation σ and maximum of the deviations (in %) of the respective path were calculated.

It was decided that neither the maximum deviation nor the mean+3σ for any given path should exceed 1%. The calculations showed (see Figure 1.13) that a `cell_size_at_quartz_surface` of **2 mm** is sufficient to keep both those values well below 1% for the paths 1-4. Consequently, this value was used for all fluence rate calculations.

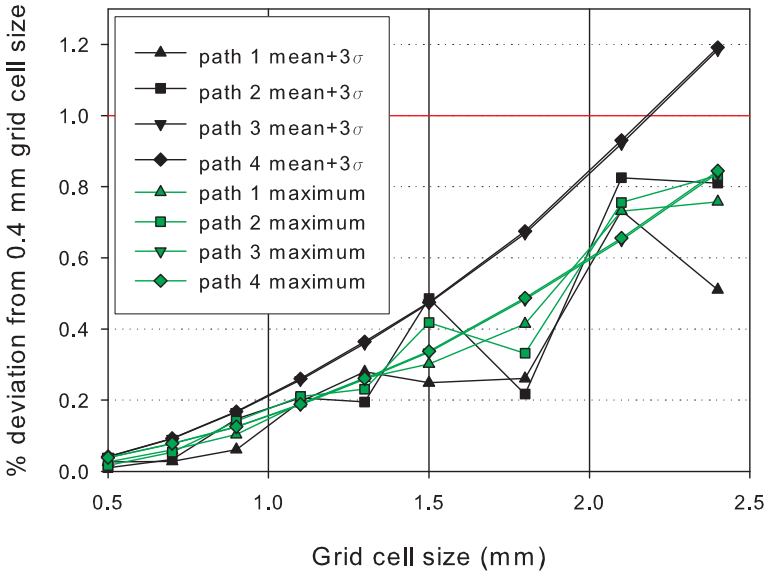

Figure 1.13.: Refinement results for `cell_size_at_quartz_surface`. The deviation of the fluence rate values from the results for $0.4\,mm$ cell size was calculated for paths 1-4. The maximum and mean+3σ of those deviations is plotted. It is found that a `cell_size_at_quartz_surface` of $2\,mm$ is sufficient to keep both those values well below 1% for the paths 1-4.

Fluence rate calculation - MPSS/MSSS models

After generating the grid, the fluence rate value for every grid point has to be calculated. The used method depends on the radiation model used.

For the MPSS and MSSS models, it is necessary to calculate the refraction angles. Since equation (1.28) cannot be solved analytically, it is transformed into the function

$$f(\theta_1) = r_1 \tan\theta_1 + n_1 \sin\theta_1 \left[\frac{r_2}{\sqrt{n_2^2 - n_1^2 \sin^2\theta_1}} + \frac{r_3}{\sqrt{n_3^2 - n_1^2 \sin^2\theta_1}} \right] - \Delta x. \tag{1.57}$$

The root of this function is found by using Brent's Method as described in [39, section 9.3]. The angle of a direct line from the lamp source to the grid point provides a lower bracket value for θ_1, while the maximum possible angle, which is calculated from the geometrical parameters, provides an upper bracket value.

When θ_1 has been found with sufficient accuracy, all other relevant variables are easily calculated, and the fluence rate contribution for the point source in question is obtained. The fluence rate at the grid point in question is then the sum of fluence rate contributions over the whole lamp. To determine the number of sources (`number_of_sources` parameter in the config file) necessary for an accurate fluence rate calculation, a refinement study was conducted at the points 1-4. The fluence rate at these points was calculated using an MSSS-F model with an increasing number of sources ranging from 10 to 10000. Afterwards, it was decided that to be sufficiently accurate, the calculated fluence rate at any point should not deviate by more than 1% from the value for 10000 sources, which was deemed to sufficiently represent the fluence rate for $N \to \infty$.

The results (see Figure 1.14) showed that to fulfill this criterion for all 4 points, **2000 sources** are necessary.

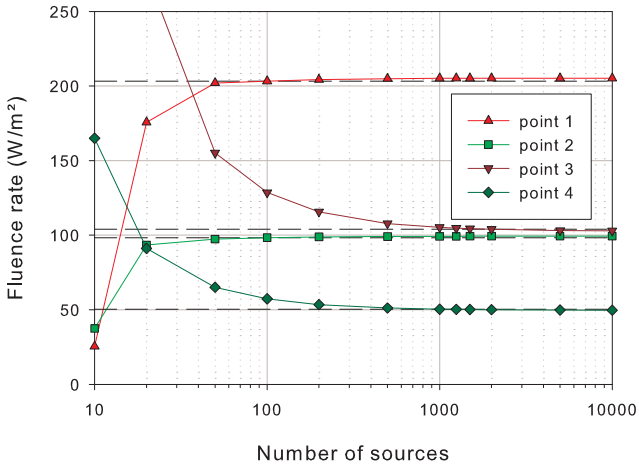

Figure 1.14.: Refinement results for `number_of_sources` for the MPSS/MSSS models. The fluence rate values for a varying number of sources is shown for paths 1-4. The dashed lines indicate the allowable deviation from the 10000 sources value.

Fluence rate calculation - LSI models

For the LSI models, an appropriate number of sources had to be chosen for an accurate calculation of the attenuation factor and consequently the fluence rate. Since an advantage of LSI models over MPSS/MSSS is the greatly reduced computational cost, choosing 2000 sources is impracticable because it would neutralize this advantage. Liu suggested in [9], that 5 sources are sufficient for LSI models. However, since this value strongly depends on the reactor geometry, a new value had to be determined for our reactor. When plotting fluence rate values of axial paths, it turns out that an insufficient number of sources leads to unnatural oscillations in the fluence rate distribution.

Since these oscillations are worst at small distances to the lamp, path 5 has been chosen for this evaluation, because it lies directly at the surface of the quartz sleeve, the nearest region accessible to particles flowing through the reactor. Figure 1.15 shows the fluence rate distribution for a varying

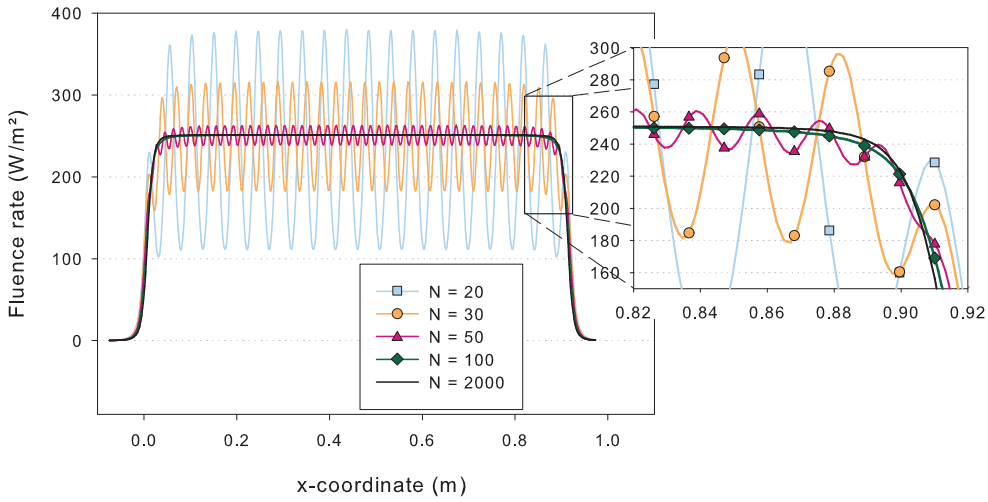

Figure 1.15.: Refinement results for `number_of_sources` for the LSI models. The fluence rate values for a varying number of sources are shown for the worst-case path 5. The inset displays a critical region to illustrate the oscillation strength for different N. At $N = 100$, no visible oscillations occur.

number of sources N with an LSI-F model. Unnatural oscillations can clearly be recognized for lower N. For the sake of clarity, symbols have only been drawn for the inset, and have been omitted for the $N = 2000$ case. The inset shows a critical region where the oscillation strength for different N can be analyzed. It was deemed that $\mathbf{N = 100}$ (green line with $\diamond$) is a sufficient number of sources to eliminate unwanted oscillations.

A computation with a RADLSI model showed analogous, but significantly weaker oscillations and is therefore not presented as a figure.

Sensor irradiance calculation

The location and direction of the sensor, as specified in the *.cfg* file, are values for the midpoint of the window surface in contact with water, and the optical axis of the sensor, respectively.

A fluence rate file (*.int*) is created which contains the data from the configuration file, the radiation grid coordinate data, the calculated sensor reading and the fluence rate values for all grid points.

1.5.3. Fluence calculation

The *.int* file is used in conjunction with the *.p*xx file which contains the particle tracking data to calculate the fluence received by every particle.

As a first step, the fluence rate at a certain particle position as given by the particle tracking file is linearly interpolated from values of the next-neighbor grid points of the fluence rate file. Due to the radial symmetry of the fluence rate field, interpolation only has to be performed in a plane of constant azimuthal angle ϕ, thereby greatly simplifying the process since 3D interpolation in a grid of cylindrical symmetry is quite difficult.

To locate the appropriate grid points, the `hunt` routine from [39, section 3.4] was adapted. This routine implements an improved version of the bisection algorithm which is much faster than bisection if a good "first guess" is available. Since the fluence calculation routine wanders along the particle path, the coordinates of the previous step yield indeed a very good guess, thereby improving computational performance significantly.

When the interpolated fluence rate value has been determined, the fluence for the current path segment is calculated as

$$H'_i = \frac{E'_i + E'_{i-1}}{2}(t_i - t_{i-1}) \tag{1.58}$$

where i is the position index of the particle path, E'_i the interpolated fluence rate and t_i the time at particle path point i. The total received fluence for one particle is then the sum over all fluence contributions along the path

$$H' = \sum_i H'_i \tag{1.59}$$

This value is calculated for all tries of particles, and written into a *.his* file, along with configuration file information.

1.5.4. REF and fluence histogram

To be able to accurately calculate the REF, a sufficient number of particle tracks has to be simulated to minimize statistical errors. Otherwise, statistical fluctuations especially of the number of particles with a low received fluence can result in significant fluctuations in the resultant REF.

To determine the necessary number of tries, the REF was calculated for one case (2B1) using 2 to 20 tries. As can be seen in Figure 1.16, **16 tries** are a reasonable compromise between accuracy and computational demand. While more tries are always desirable, 16 tries nearly exceeded the available computational capacity: The resultant particle files are about 13 GB large and typically contain 26656 particle tracks.

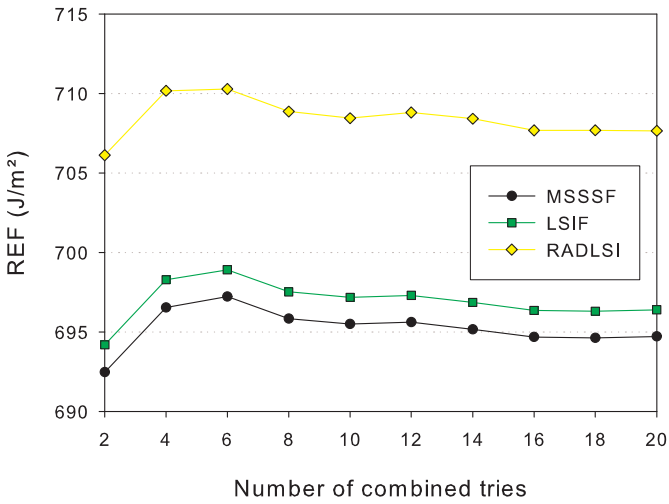

Figure 1.16.: Refinement results for the number of tries. The REF values for a varying number of tries are shown for case 2B1. 16 tries are a reasonable compromise between accuracy and computational demand. Only three radiation models are shown, the others show analogous behavior.

The resultant fluence distribution contained in a *.his* file can be used to plot a fluence histogram. By means of this histogram, particles with exceptionally high or low fluence can easily be identified, and consequently

the paths of those critical particles be plotted to identify problematic regions (e.g. short-circuits through the reactor vessel).

2. Results and Discussion

In this chapter, the obtained results are presented, summarizing the whole workflow. Section 2.1 visualizes important flow phenomena occurring in the reactor and deals with the relevant results from the CFD calculations. Section 2.2 contains an evaluation of the different implemented radiation models, while in section 2.3, the results for the total disinfection simulation are presented and compared to the certification reports.

2.1. CFD

To illustrate the main flow characteristics, one case (2B1) of medium flow rate ($\approx 3.5\,m^3/h$) has been chosen. Several figures display standard post-processing parameters to aid the reader in understanding the flow characteristics in the UVD reactor. To keep this section clear, these big figures are placed in the appendix, so please find them in section A.2, beginning on page 81.

Figure A.2 displays a view of the whole simulated reactor. Path lines colored by velocity magnitude are included in the view. Path lines, although very similar in our case, are not to be confused with particle tracks. They just indicate the direction of the local flow velocity, without regarding particle equations of motion or random effects. They are, however, a good tool to visualize flow in the UVD reactor. For better illustration, the inner walls have been rendered, while walls obstructing the view into the calculation domain have been removed. Water enters the reactor assembly in the bottom left corner of the figure, flows through the **elbow**, enters the **reactor chamber** at the **reactor inlet**, flows upwards and consequently exits the chamber through the **reactor outlet** and exits the computational domain at the end of the outlet pipe. A spiral character of the flow in the reactor chamber is clearly visible.

This helical flow is created by the asymmetric velocity profile at the reactor inlet created by the upstream elbow. This is clarified in Figure A.3. The flow entering at the bottom is being deflected by the elbow. Its momentum causes the velocity distribution at the end of the elbow to become asymmetric.

Furthermore, a characteristic secondary flow in the elbow is also visible: Two counter-rotating vortices form perpendicular to the flow direction in the elbow. This phenomenon can easily be recognized in Figure A.4, which displays an oil-flow visualization on the elbow wall, colored by particle ID.

Figure A.5, looking in flow direction, plots velocity vectors projected onto a cross-section plane at the end of the elbow, which also makes the two vortices visible. The vectors are colored by velocity magnitude.

The asymmetric inflow into the reactor chamber causes a helical motion of water in the cylindrical chamber. Figure A.6 depicts this phenomenon. The number of plotted pathlines has been reduced for clarity.

To judge the influence of said elbow, an additional model has been created, where the elbow is replaced by a straight pipe of equal length. This model has been simulated for case 2B1, and will be called "2B1str". It has been found that the pressure loss in the reactor is reduced by 6.6% by this modification. See Table 2.1 on page 65 for details. The influence of this modification on the disinfection performance is treated in section 2.3.4.

The only parameter provided by the ÖNORM certifications [30–32] to check the CFD computations against was the pressure loss of the system. This is because velocity distribution measurements are not part of the certification process.

Excellent agreement with the experimental results was reached. It should be noted that the calculations for the realizable k-ϵ ($rk\epsilon$) turbulence model, which form the bulk of calculations, have been carried out in steady state. It may be that there occur significant fluctuations in the water flow, which influence disinfection results, but cannot be reproduced by steady-state calculations. Unfortunately, unsteady calculations were computationally too expensive, especially in light of potential future industry applications of UV disinfection simulation. Thus, only a small number of unsteady calculations have been performed with the DES turbulence model.

Figure 2.1 directly compares experimental and numerical results. Experimental results from [30–32] and additional measurements by Georg Hirschmann are displayed along with a quadratic fit ($R^2 = 0.9981$) of these data. CFD results from two different turbulence models are also plotted to show the excellent agreement between experimental and numerical results.

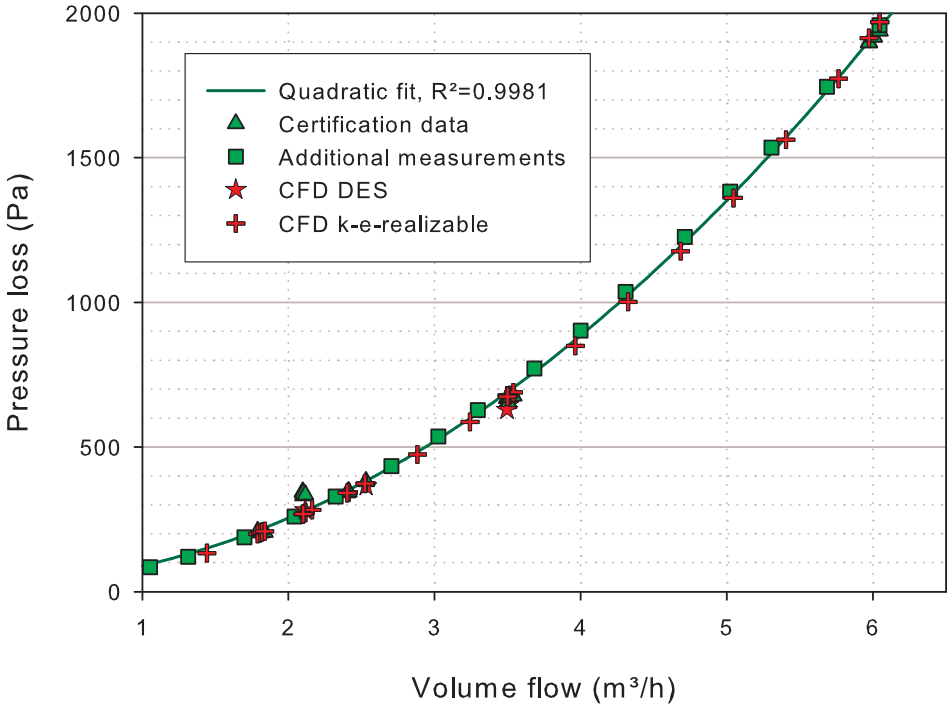

Figure 2.1.: pressure loss (Pa) of the UVD system vs. volume flow rate (m^3/h). Experimental data for different measurements and their quadratic fit are plotted. Furthermore, CFD results from two different turbulence models are shown. They show excellent agreement with the experimental data.

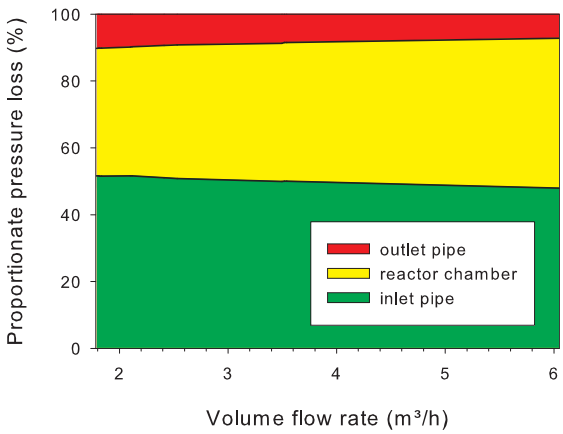

Figure 2.2.: Proportionate pressure loss of the UVD system vs. volume flow rate, from $rk\epsilon$ CFD calculations. The inlet pipe system is responsible for $\approx$ 50% of the pressure loss. With increasing volume flow rate the contribution of the central reactor chamber rises slightly.

Figure 2.2 depicts the proportionate pressure loss in the different sections of the UVD system. The section from the inlet pressure sensor to the reactor inlet (the *inlet pipe*) is responsible for $\approx$ 50% of the pressure loss. The contribution of the central *reactor chamber* rises slightly with increasing volume flow rate. Replacing the elbow with a straight pipe (case 2B1str) reduced the proportion of the inlet pipe from 50 to 43%, while the proportion of the reactor chamber rose from 41 to 47%. The section from the reactor outlet to the outlet (the *outlet pipe*) makes up a rather small portion of the overall pressure loss.

Table 2.1 displays the results of the CFD calculations and their deviation from the experimental results and the fit. For 4 cases, DES calculations have been conducted. These cases are marked with the suffix "D". Note that the cases with $\dot{V}$ around $2.1\,m^3/h$ show a rather big deviation from the experiment, but agree well with the fit.

Table 2.1.: Pressure loss results. The CFD simulation results are given. $\dot{V}$ is in m^3/h and *pressure loss* is in Pa. *Error* gives the relative error of the CFD calculation relating to the experimental results† and the fit‡, respectively. *Section press.* (Pa) shows the simulated pressure at the reactor inlet (p_{RI}) and the reactor outlet (p_{RO}).

	$\dot{V}$	pressure loss			Error (%) to		Section press.	
		exp.	fit	CFD	exp.†	fit‡	p_{RI}	p_{RO}
1A1	2.401	342	348.8	341.1	**-0.3**	**-2.2**	166.9	31.9
1A2	1.820	205	217.4	205.6	**0.3**	**-5.4**	99.6	20.9
1A2*	1.837	206	220.8	209.2	**1.6**	**-5.2**	101.4	21.2
1A1*	2.411	346	351.4	343.4	**-0.8**	**-2.3**	168.1	32.1
1B1	2.531	381	382.8	375.2	**-1.5**	**-2.0**	184.5	34.6
1B1D	2.531	381	382.8	365.6	**-4.0**	**-4.5**	205.3	25.7
1B2	1.809	204	215.3	203.2	**-0.4**	**-5.6**	98.4	20.7
1B2*	1.789	209	211.4	199.1	**-4.7**	**-5.8**	96.4	20.3
1B1*	2.410	345	351.1	342.9	**-0.6**	**-2.3**	167.9	32.0
2A1	3.540	677	704.9	689.1	**1.8**	**-2.2**	344.5	58.6
2A2	2.097	345	275.8	267.4	**-22.5**	**-3.1**	129.5	26.0
2A2*	2.101	340	276.7	268.6	**-21.0**	**-2.9**	130.0	26.2
2A1*	3.504	656	691.6	678.6	**3.4**	**-1.9**	339.1	58.1
2B1	3.496	668	688.7	677.8	**1.5**	**-1.6**	339.4	58.8
2B1str	3.496	668	688.7	632.9	**-5.3**	**-8.1**	359.4	63.3
2B1D	3.496	668	688.7	629.1	**-5.8**	**-8.7**	351.5	41.9
2B2	2.115	335	279.9	272.9	**-18.5**	**-2.5**	132.0	26.6
2B2D	2.115	335	279.9	281.8	**-15.9**	**0.7**	166.6	20.4
2B2*	2.100	332	276.5	269.1	**-18.9**	**-2.7**	130.2	26.4
2B1*	3.503	668	691.3	675.7	**1.2**	**-2.3**	337.8	57.5
3A1	6.047	1938	1948.4	1969.2	**1.6**	**1.1**	1024.4	141.6
3A1D	6.047	1938	1948.4	2081.2	**7.4**	**6.8**	1219.0	101.3
3A2	3.500	650	690.2	674.3	**3.7**	**-2.3**	337.1	57.3
3A2*	3.506	652	692.4	676.1	**3.7**	**-2.3**	338.1	57.4
3B1	5.974	1899	1903.2	1913.9	**0.8**	**0.6**	994.2	139.2
3B2	3.502	656	690.9	674.9	**2.9**	**-2.3**	337.4	57.3
3B2*	3.517	672	696.4	679.5	**1.1**	**-2.4**	339.9	57.5
3B1*	5.974	1899	1903.2	1913.9	**0.8**	**0.6**	994.2	139.2

2.2. Radiation models

The radiation models which have been implemented in the REF calculation are: **MPSS-F**, **MSSS**, **MSSS-F**, **LSI-F** and **RADLSI**. MPSS-F, MSSS-F and MSSS have been included to judge the influence of the point source approximation and the focus effect on the resultant radiation field. RADLSI and LSI-F are compared to the physically most accurate MSSS-F to see if one can maintain calculation accuracy while significantly reducing computational effort.

The paths and points for radiation evaluation have already been presented in figure 1.12 in section 1.5.2. In the following, the fluence rate distributions of different radiation models are evaluated at the paths 1-4 for the case 2B1. It was determined beforehand that the distributions for other cases exhibit similar behavior, thus only one case is presented here.

Due to the lack of detailed experimental data for validation of the radiation models, the different models can only be compared among themselves. Figures 2.3, 2.4, 2.5 and 2.6 show the results of the radiation evaluation.

Figures 2.3 to 2.5 show an excellent agreement between the MSSS-F (black circles) and LSI-F models (green squares). This is consistent with findings in [9]. A slight deviation exists when approaching the ends of the lamp. It becomes noticeable in the axial plots shortly before fluence rate values begin to drop rapidly. This deviation is the reason why in Figure 2.6, which displays a radial plot at the end of the lamp, the LSI-F and MSSS-F plots are slightly apart.

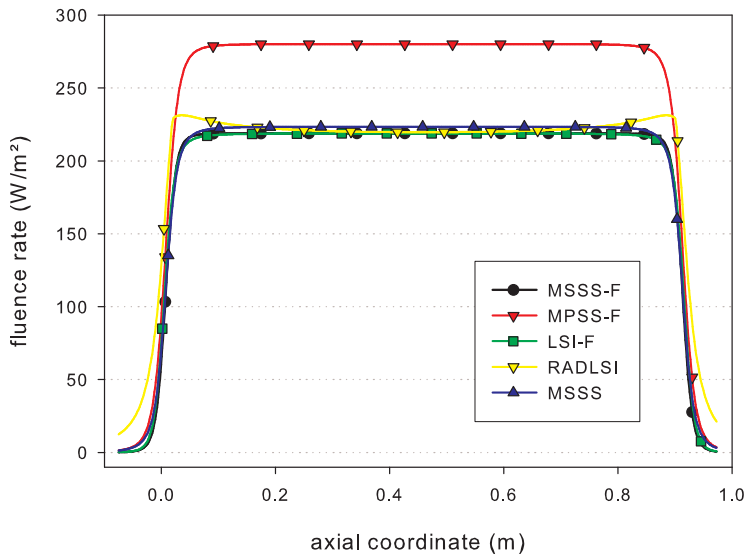

Figure 2.3.: Fluence rate distribution for case 2B1, path 1.

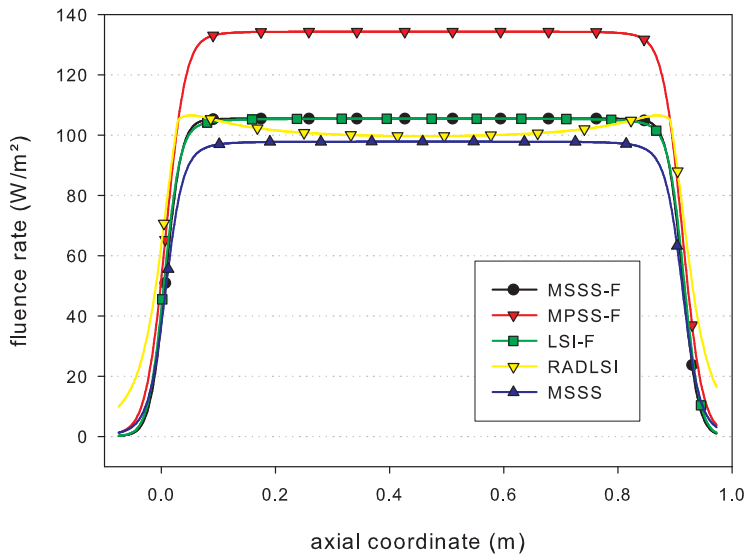

Figure 2.4.: Fluence rate distribution for case 2B1, path 2.

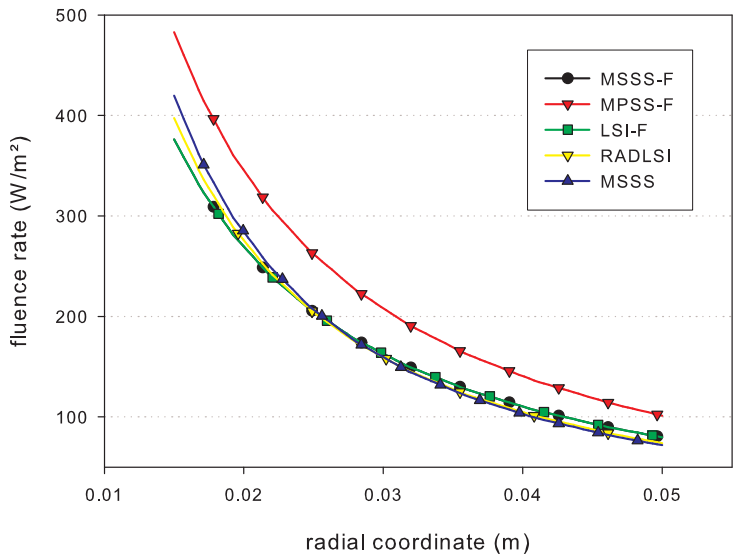

Figure 2.5.: Fluence rate distribution for case 2B1, path 3.

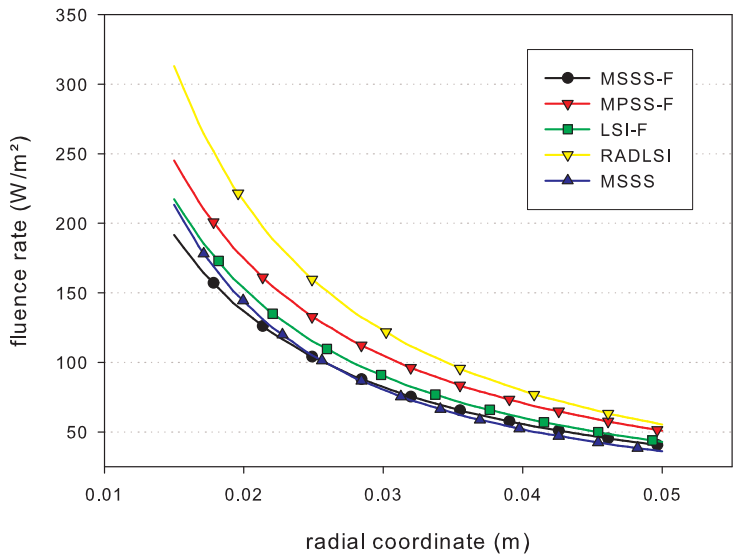

Figure 2.6.: Fluence rate distribution for case 2B1, path 4.

Considering that calculating a fluence rate field for the reactor with the MSSS-F model takes approximately 17 times as long as with a LSI-F model, using the LSI-F model seems to be highly tempting. However, one should keep in mind that the fluence rate calculation takes a rather small part of the computation time compared to particle track generation and particle fluence calculation, especially for a high number of particle tracks.

When comparing the MSSS, MSSS-F and MPSS-F results, it can be concluded that the influence of the focus effect (i.e. the difference between MSSS and MSSS-F) is far smaller than the influence of the segment source representation (i.e. the difference between MPSS-F and MSSS-F). Thus, it was concluded that implementing segment sources is definitely necessary. Fortunately, this does not measurably increase computation time, and thus has no drawbacks.

It is recommended to use either the MSSS-F or the LSI-F model for calculating the fluence rate distribution in an UVD reactor of the examined type.

When simulating other reactors, especially types with a very high number of lamps, which significantly increases the time necessary for the fluence rate calculation, it may be unavoidable to use the LSI-F model. Due to the fact that both models show a nearly identical behavior, this seems acceptable. Nevertheless, it should be confirmed that this nearly identical behavior is still valid for another reactor.

2.3. Disinfection results

Disinfection calculations have been conducted for all cases in Table 2.1, except the DES calculations, and for all radiation models treated in section 2.2. The disinfection performance is expressed by the REF value a certain case reached. The achieved REF value depends on the particle tracks (influenced by the fluid flow resulting from the CFD simulation) and on the fluence rate distribution. 3 input parameters can be controlled: The volume flow, the lamp radiation power (expressed as the product of lamp power rating and UV efficiency) and the transmittivity of the water. The influence of the reactor geometry has been tested with case 2B1str.

2.3.1. REF results

Figure 2.7 shows the REF values obtained with the UVD simulation. Black crosses are the experimental results with error bars from [30–32]. The different results have been connected with lines only to guide the eye and facilitate analysis.

As expected from the fluence rate distributions, the MPSS-F model generally produces the highest REF values. All other plots typically are very close together. Also, MSSS-F and LSI-F produce nearly identical results. The MSSS-F plot is not visible because it lies behind the LSI-F plot. This further confirms that the LSI-F model is a good approximation of the MSSS-F model.

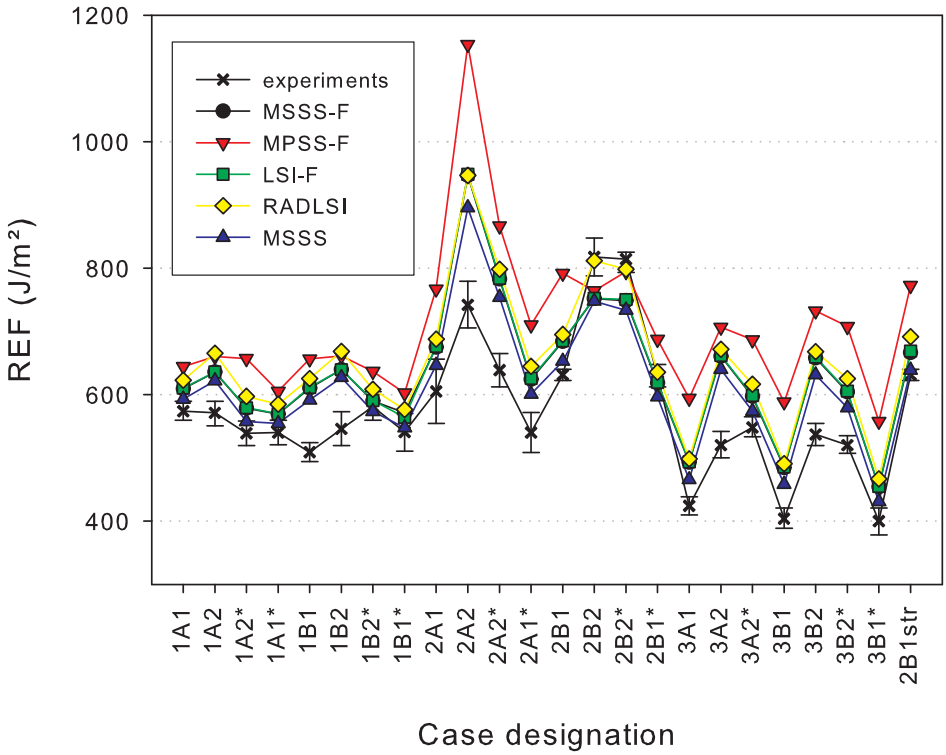

Figure 2.7.: Disinfection simulation results: REF. The simulated REF values for the different cases and experimental results with error bars are shown. Connecting lines have been added to ease analysis.

2.3.2. REF error

Figure 2.8 shows a plot of the relative errors of the different radiation models. An analysis of the error value distribution has been done. Mean value and standard deviation of the error have been calculated for all radiation models and cases, excluding case 2B1str because it has a different geometry. The results can be found in Table 2.2.
The MSSS model produces the smallest mean error, and also the smallest standard deviation. MSSS-F and LSI-F rank next, producing virtually identical results. RADLSI comes next, and MPSS-F produces the least accurate results. However, one has to keep in mind that the UV efficiency was used to calibrate the radiation models such that the experimental reference sensor reading is matched by the MSSS-F model. A different UV efficiency value would shift all REF results up or down, thus changing the error values and the ranking of the different radiation models.

The consistently positive mean values show that all radiation models generally over predict the REF values. This over prediction may be corrected by shifting the resultant REF values by a certain value. However, the amount of this shift may be influenced by e.g. geometry, and thus cannot be assumed to be generally valid.

Table 2.2.: REF simulation error statistics. Mean value and standard deviation of REF simulation errors (in %) are given for different radiation models.

	MSSS-F	MPSS-F	LSI-F	RADLSI	MSSS
mean	11.58	24.65	11.71	14.64	7.54
std. deviation	9.9	15.37	9.97	9.06	8.93

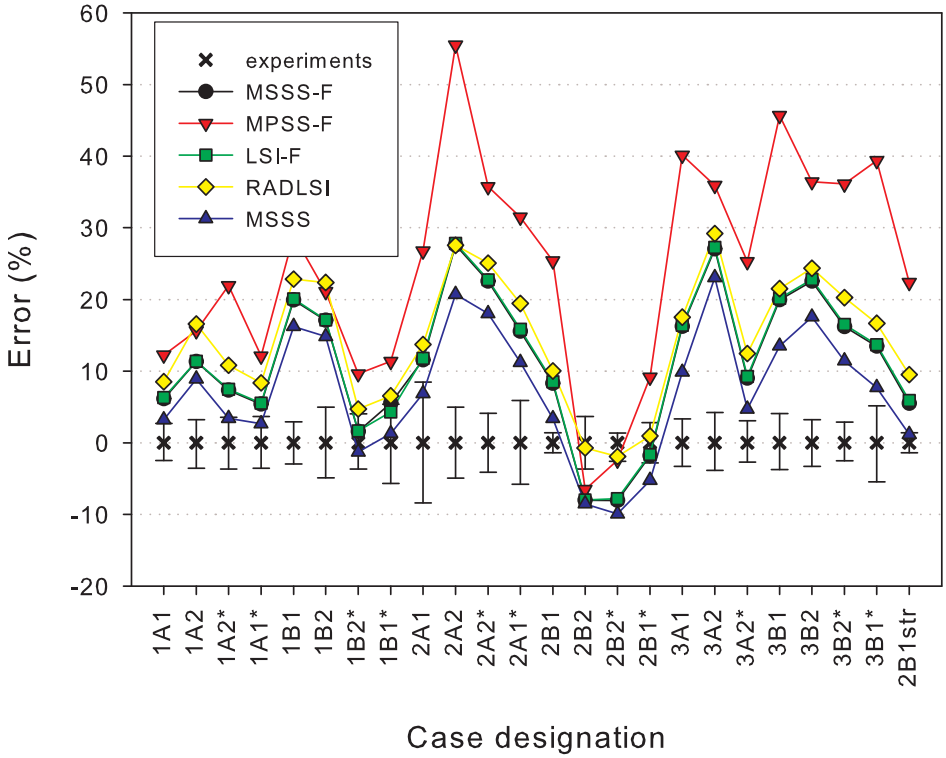

Figure 2.8.: Disinfection simulation results: relative error. The relative error is plotted for the different cases. Connecting lines have been added to ease analysis.

2.3.3. Biodosimetric vs. simulated REF

Figure 2.9 shows a plot of the simulated vs. the biodosimetric REF results for the different radiation models. A linear fit has been added to the plot. The fit parameters can be found in Table 2.3. To indicate the biodosimetric REF uncertainty given in [30–32], error bars have been added in the lower part of the plot. Every error bar corresponds to one case. They have been arbitrarily staggered to preserve clarity. The MSSS-F and LSI-F fit lines are again identical. The data point group at a biodosimetric REF of $\approx 740\,J/m^2$ belongs to case 2A2, which is the one with the worst error, according to Figure 2.8.

An ideal fit line would have an offset d of 0 and a slope k of 1, which would mean that experimental and simulated REF are identical. Keeping this in mind, it is notable that all the lines have a significant offset. This again indicates that a change in the set UV efficiency, which would proportionately influence the simulated REF and thus vertically shift the fit curves, could be used to improve the simulation error.

The slope for all models except RADLSI is very similar at around 0.81.

However, one should keep in mind that the data are quite scattered and cover a rather low REF range. Also, the obtained R^2 values are quite low. This gives reason to treat the above findings with caution. For better results, more data would have to be obtained, and optimally a greater REF range would have to be covered. Unfortunately, industrial UVD reactor design aims to keep the REF as low as possible, but still above $400\,J/m^2$ to minimize operation costs.

2.3.4. Straight inlet pipe

For the case 2B1str, a disinfection simulation has been performed. The REF values for the different radiation models show an average drop in REF of 2% compared to the case 2B1. This REF change does not seem to be significant, as it most probably lies inside the error region of the simulation process.

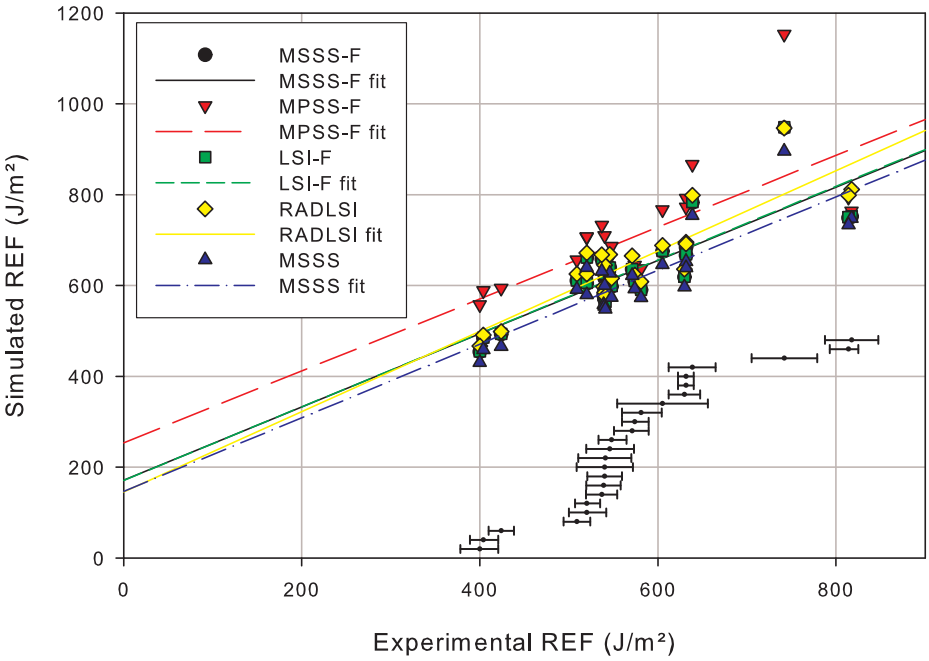

Figure 2.9.: Simulated vs. biodosimetric REF results are plotted for the different radiation models. A linear fit has been added. To indicate the biodosimetric REF uncertainty, error bars have been included in the lower part of the graph.

Table 2.3.: Simulated vs. biodosimetric REF fit coefficients. The goodness of fit R^2, the slope k and the offset d are given for the different radiation models.

	MSSS-F	MPSS-F	LSI-F	RADLSI	MSSS
R^2	0.689	0.476	0.688	0.768	0.734
k	0.81	0.79	0.81	0.88	0.82
d	171	253	171	146	147

2.3.5. Fluence histograms

Using the data from the UVD simulation, fluence histograms can easily be generated. Figure 2.10 displays a typical histogram, showing the fluence distribution for case 2B1 using the MSSS-F model. The resultant REF and arithmetic mean of the fluence distribution are shown to demonstrate the difference between mean and REF as explained in section 1.4.10. The x-axis scale has been limited to 3000 J/m^2 to improve display of the relevant portion of the fluence histogram. Actual fluence values reach up to 5200 J/m^2, but the particle counts are negligibly small above the chosen limit.

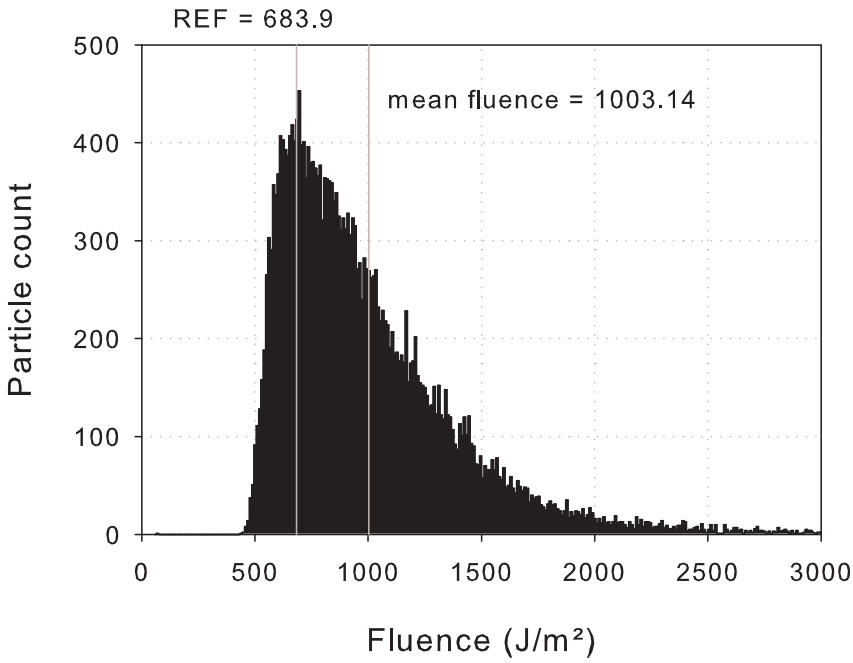

Figure 2.10.: Fluence histogram for case 2B1 and MSSS-F model. The resultant REF and arithmetic mean of the fluence distribution are indicated.

3. Conclusions

A simulation method to predict UV reactor disinfection performance has been presented.

CFD calculations have been performed for a small UV disinfection reactor. 24 different sets of operation parameters have been simulated.
The pressure loss of the UVD system was obtained with an average accuracy of $\approx 5\%$.

The movement of microorganisms through the reactor has been simulated with a particle tracking model including turbulence effects.

5 different radiation models have been implemented, and radiation fields were calculated for the reactor. Refinement studies have been made, resulting in certain necessary grid resolutions and lamp discretization parameter values, which are reactor-dependent. The MSSS-F radiation model is recommended for use due to its accurate representation of the physical processes involved. The LSI-F model is recommended because it exhibits a behavior nearly identical to MSSS-F, while needing significantly less computation time.

Obtained data were combined to calculate the received fluence of every particle. From this data, the reduction equivalent fluence was obtained. It has been found that a significant amount of simulated particles (≈ 26000) is necessary to gain a reliable statistical base for REF calculations.

REF Results were compared to available biodosimetric measurements to assess the accuracy of the simulation. Considering the limited amount of available experimental data for the flow field and fluence rate distribution, good predictions of the REF were obtained. Average error values varied between 7 and 25%, depending on the chosen radiation model. Simulations

have been done for a slightly different geometry, and fluence histograms have been calculated, showing the advantages of simulation over classical biodosimetric analysis.

The potential use of this method for designing and improving UVD reactors has been demonstrated.

Future work will encompass unsteady CFD calculations, which will yield unsteady particle tracks. Furthermore, different reactor geometries can be examined. Further investigations into the UV conversion efficiency of the lamp are desirable. Ray-tracing can additionally be employed to include reflection at the reactor walls, and the influence of diffraction on the disinfection efficacy can be examined.

A. Appendix

A.1. Data processing

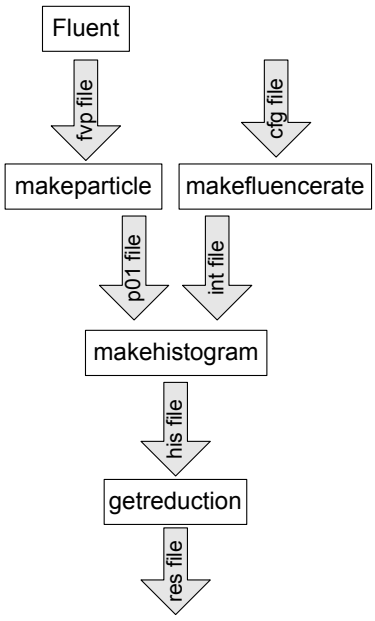

Figure A.1.: Flow diagram of the simulation procedure.
Fluent is used to calculate the water flow and particle tracks. An `fvp` file is used to pass particle tracks to `makeparticle`, which converts the particle tracks into a streamlined `p01` file. The `cfg` configuration file is passed to `makefluencerate` to generate an `int` file containing the fluence rate distribution in the reactor vessel. `makehistogram` combines the `p01` and `int` files to calculate the received fluence values for every particle, and stores this information in a `his` histogram file. `getreduction` is used to calculate the reduction and REF from the fluence histogram and store these results in a `res` file, which marks the end of the simulation process.

Table A.1.: Meaning of the configuration file parameters

Parameter	Typical value	Meaning
`model`	MPSS	Abbreviation of the radiation model to be used
`r1`	0.013	Inner radius of the quartz sleeve
`r2`	0.002	Outer radius of the quartz sleeve
`r3`	0.035	Inner radius of the reactor vessel wall
`n1`	1	Refractive index of air
`n2`	1.506	Refractive index of the quartz sleeve
`n3`	1.376174	Refractive index of water
`cell_size_at_quartz_surface`	0.002	Basic cell size of the fluence rate data grid
`number_of_sources`	2000	Number of sources for radiation models
`lamp_power`	80	Electrical power rating of the UV lamp
`UV-efficiency_254`	0.4	Efficiency of conversion of electric power to UV light
`reactor_begins_x`	-0.075	Minimum axial coordinate of the reactor vessel
`reactor_ends_x`	0.973	Maximum axial coordinate of the reactor vessel
`lamp_begins_x`	0.008	Minimum axial coordinate of the UV lamp
`lamp_ends_x`	0.913	Maximum axial coordinate of the UV lamp
`T10_1`	1.0	$10\,mm$ transmittance of air
`T10_2`	0.8208	$10\,mm$ transmittance of the quartz sleeve
`T10_3`	0.9124	$10\,mm$ transmittance of water
`sensor_position_x`	0.444	x-coordinate of the UV sensor
`sensor_position_y`	0	y-coordinate of the UV sensor
`sensor_position_z`	-0.05	z-coordinate of the UV sensor
`sensor_direction_x`	0	x-value of the UV sensor direction vector
`sensor_direction_y`	0	y-value of the UV sensor direction vector
`sensor_direction_z`	1	z-value of the UV sensor direction vector
`th4`	0.005	Thickness of the quartz sensor window
`th5`	0.001	Thickness of the air gap between sensor and window
`n4`	1.506	Refractive index of the quartz sensor window
`n5`	1.0	Refractive index of the air gap between sensor and window
`T10_4`	0.8208	$10\,mm$ transmittance of the quartz sensor window
`T10_5`	1.0	$10\,mm$ transmittance of the air gap

A.2. CFD results

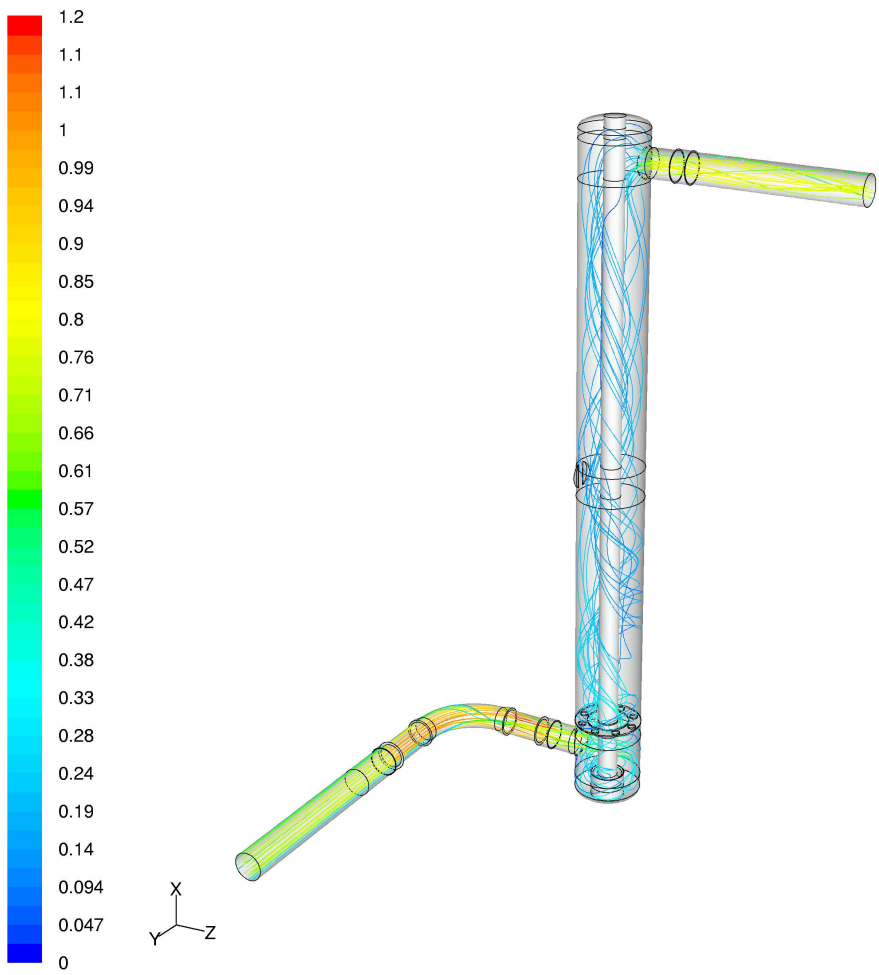

Figure A.2.: Path lines for the whole reactor. Lines are colored by velocity magnitude (m/s). In this and the following figures, the sidebar indicates the values associated with a certain color. The spiral flow character in the main reactor is clearly visible.

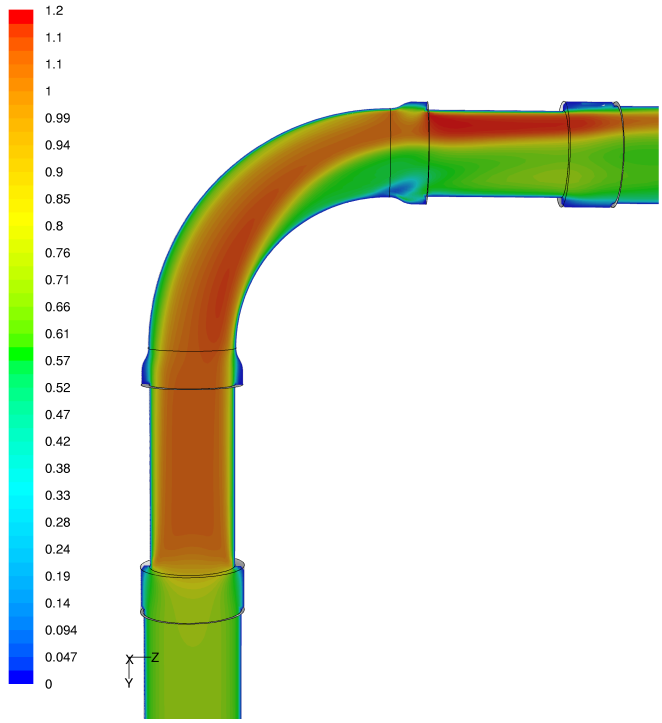

Figure A.3.: Velocity magnitude (m/s) in the elbow. Clearly visible is the asymmetric velocity distribution downstream of the elbow.

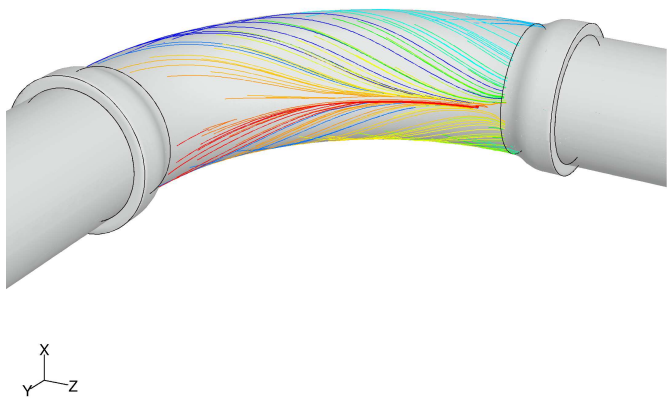

Figure A.4.: Oil flow visualization in the elbow, colored by particle ID. This Figure visualizes the velocity direction at the elbow wall, thus making two counter-rotating vortices visible. The flow direction is left to right.

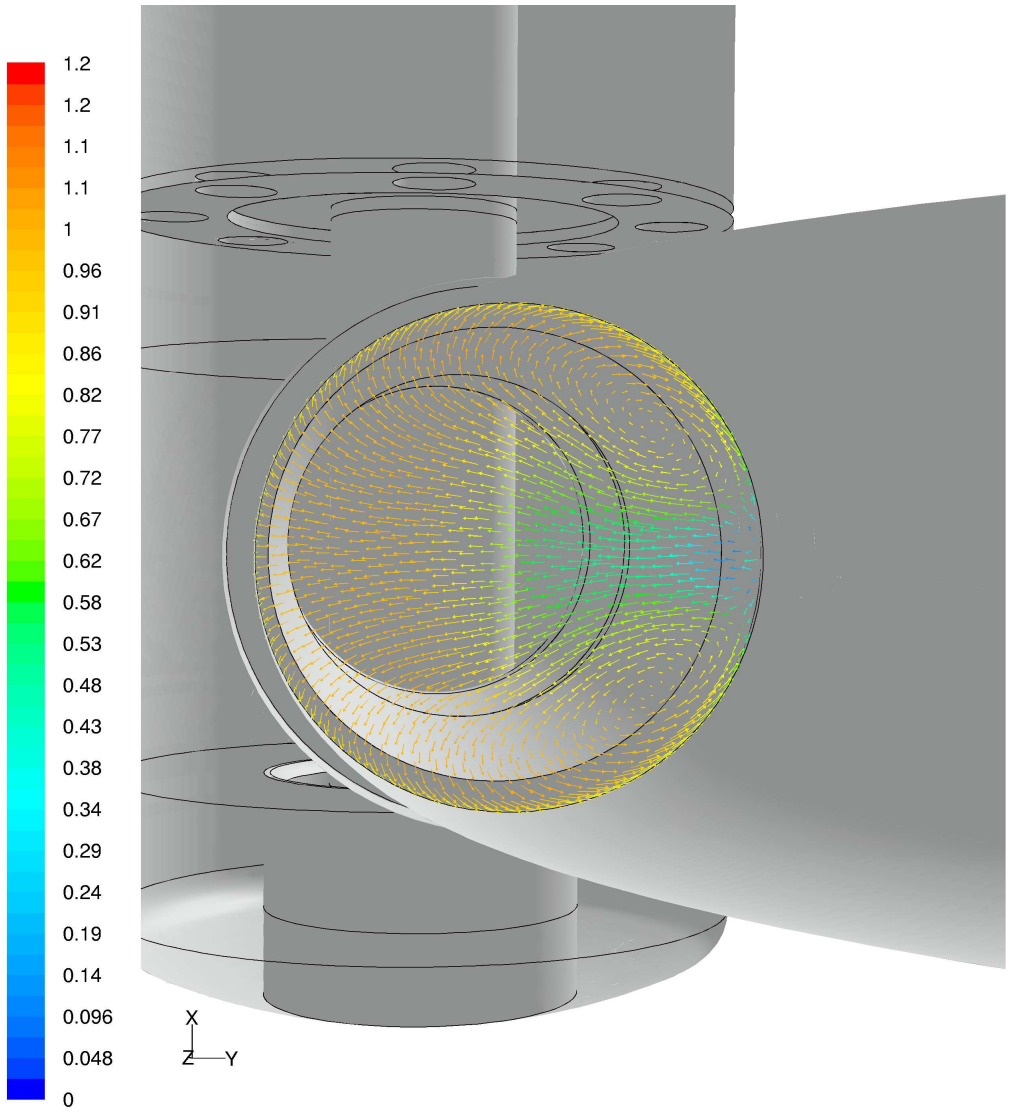

Figure A.5.: Velocity vectors in the elbow cross-section, colored by velocity magnitude (m/s). Two counter-rotating vortices are visible

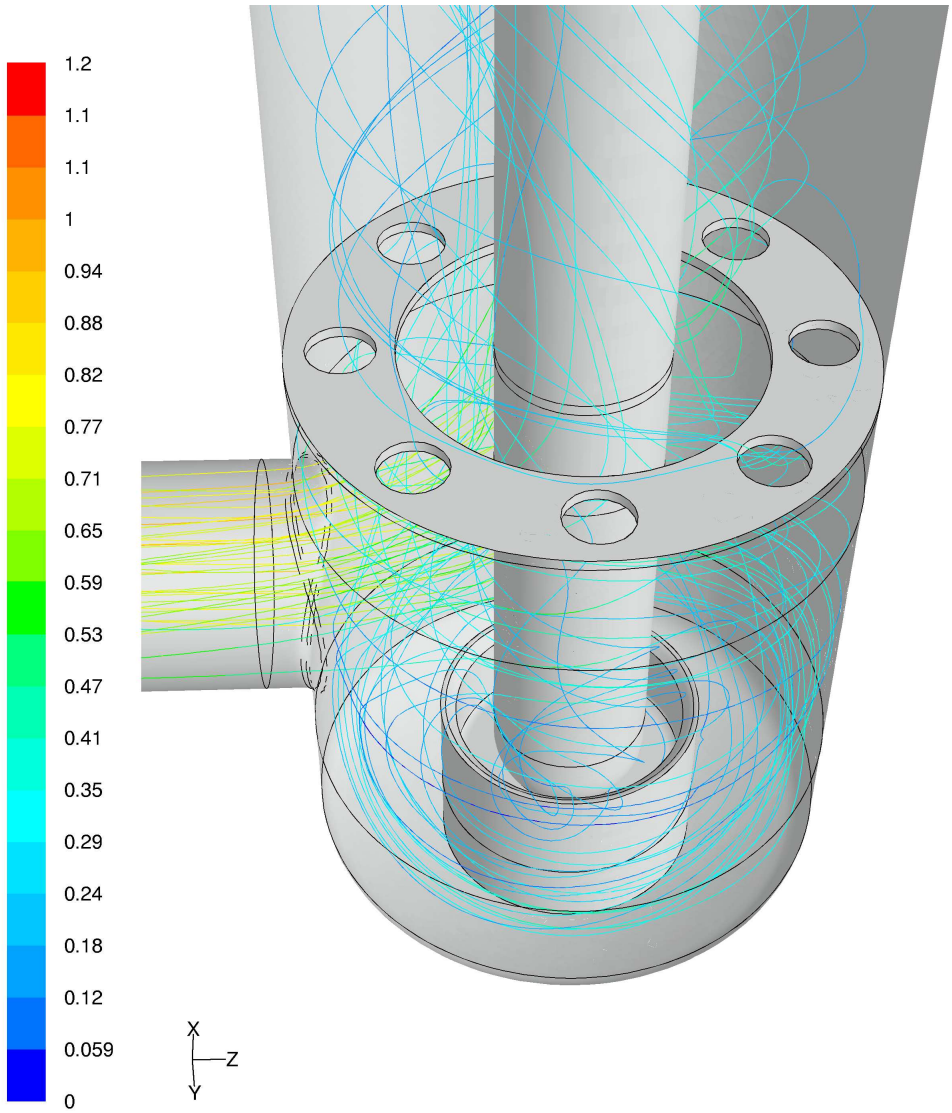

Figure A.6.: Path lines for the inlet region. Clearly visible is how the asymmetrical inlet flow induces a helical flow. Colored by velocity magnitude (m/s).

List of Figures

List of Tables

List of Acronyms

ATCC	American Type Culture Collection
CFD	Computational Fluid Dynamics
DES	Detached Eddy Simulation
DNA	Desoxyribonucleic acid
DRW	Discrete Random Walk
LES	Large Eddy Simulation
LP	Low Pressure
LSI	Line Source Integration
LSI-F	Line Source Integration with focus effect
MP	Medium Pressure
MPSS	Multiple Point Source Summation
MPSS-F	Multiple Point Source Summation with focus effect
MSSS	Multiple Segment Source Summation with focus effect
MSSS-F	Multiple Segment Source Summation
RADLSI	Radial Line Source Integration
RANS	Reynolds-averaged Navier Stokes
REF	Reduction Equivalent Fluence
$rk\epsilon$	Realizable k-ϵ
UV	Ultraviolet
UVD	Ultraviolet Disinfection

Bibliography

[1] Gelzhäuser, Peter, Bewig, F., Holm, K., Kryschi, R., Reich, G. and Steuer, W. *Desinfektion von Trinkwasser durch UV-Bestrahlung*, volume 182 of *Kontakt & Studium*. Technische Akademie Esslingen and expert verlag, 1985.

[2] Österreichisches Normungsinstitut, 1021 Wien. *ÖNORM M 5873-1: Anlagen zur Desinfektion von Wasser mittels Ultraviolett-Strahlen - Anforderungen und Prüfung - Teil 1: Anlagen mit Quecksilberdampf-Niederdruckstrahlern*, March 2001.

[3] Bohrerova, Zuzana, Bohrer, Gil, Mohanraj, S. Mohan, Ducoste, Joel and Linden, Karl G. "Experimental Measurements of Fluence Distribution in a UV Reactor Using Fluorescent Microspheres." *Environ. Sci. & Technol.*, volume 39(22):pp. 8925–8930, 2005.

[4] Ducoste, Joel J., Liu, Dong and Linden, Karl. "Alternative Approaches to Modeling Fluence Distribution and Microbial Inactivation in Ultraviolet Reactors: Lagrangian versus Eulerian." *Journal of Environmental Engineering*, volume 131(10):pp. 1393–1403, 2005.

[5] Ducoste, Joel and Linden, Karl. "Determination of ultraviolet sensor location for sensor set-point monitoring using computational fluid dynamics." *J. Environ. Eng. Sci.*, volume 4:pp. 33–43, 2005.

[6] Jin, Shanshan, Linden, Karl G., Ducoste, Joel and Liu, Dong. "Impact of lamp shadowing and reflection on the fluence rate distribution in a multiple low-pressure UV lamp array." *Water Research*, volume 39:pp. 2711–2721, 2005.

[7] Bolton, James R., Wright, Harold and Rokjer, David. "Using a mathematical fluence rate model to estimate the sensor readings in a multi-lamp ultraviolet reactor." *J. Environ. Eng. Sci.*, volume 4:pp. 27–31, 2005.

[8] Bolton, James R. "Calculation of ultraviolet fluence rate distribution in an annular reactor: Significance of refraction and reflection." *Wat. Res.*, volume 34(13):pp. 3315–3324, 2000.

[9] Liu, Dong. *Numerical Simulation of UV disinfection reactors: Impact of fluence rate distribution and turbulence modeling*. Ph.D. thesis, North Carolina State University, 2004.

[10] Chiu, K., Lyn, D.A., Savoye, P. and III, E.R. Blatchley. "Integrated UV Disinfection Model Based on Particle Tracking." *Journal of Environmental Engineering*, volume 125(1):pp. 7–16, 1999.

[11] Downey, D., Giles, D.K. and Delwiche, M.J. "Finite element analysis of particle and liquid flow through an ultraviolet reactor." *Computers and Electronics in Agriculture*, volume 21:pp. 81–105, 1998.

[12] Buffle, Marc-Olivier, Chiu, Kuang-Ping and Taghipour, Fariborz. "UV reactor conceptualization and performance optimization with computational modeling." In "Proceedings WEF Specialty Conference on Disinfection," New Orleans, LA, 2000.

[13] Christensen, Jason and Linden, Karl G. "How particles affect UV light in the UV disinfection of unfiltered drinking water." *Journal AWWA*, volume 95(4):pp. 179–189, April 2003.

[14] Kowalski, W.J., Bahnfleth, W.P., Witham, D.L., Severin, B.F. and Whittam, T.S. "Mathematical Modeling of Ultraviolet Germicidal Irradiation for Air Disinfection." *Quantitative Microbiology*, volume 2(3):pp. 249—270, 2000.

[15] Zimmer, J.L. and Slawson, R.M. "Potential Repair of *Escherichia coli* DNA following Exposure to UV Radiation from Both Medium- and Low-Pressure UV Sources Used in Drinking Water Treatment." *Applied and Environmental Microbiology*, volume 68(7):pp. 3293–3299, July 2002.

[16] Cabaj, A., Sommer, R., Pribil, W. and Haider, T. "The spectral UV sensitivity of microorganisms used in biodosimetry." *Water Science and Technology: Water Supply*, volume 2(3):pp. 175–181, 2002.

[17] Cabaj, Alexander and Sommer, Regina. "Measurement of UV-Radiation with Microorganisms (Biodosimetry)." In Rüdiger Matthes

and David Sliney (editors), "Measurements of Optical Radiation Hazards, A Reference Book," ICNIRP, CIE, 1999.

[18] Cabaj, Alexander, Sommer, Regina and Schoenen, D. "Biodosimetry: Model calculations for UV water disinfection devices with regard to dose distributions." *Water Research*, volume 30(4):pp. 1003–1009, April 1996.

[19] Mamane-Gravetz, Hadas, Linden, Karl G., Cabaj, Alexander and Sommer, Regina. "Spectral Sensitivity of *Bacillus subtilis* Spores and *MS2 Coliphage* for Validation Testing of Ultraviolet Reactors for Water Disinfection." *Environmental Science and Technology*, volume 39(20):pp. 7845–7852, 2005.

[20] Das, Tapas K. "Ultraviolet disinfection application to a wastewater treatment plant." *Clean Products and Processes*, volume 3(2):pp. 69–80, 2001.

[21] Das, Tapas K. "Evaluating the life cycle environmental performance of chlorine disinfection and ultraviolet technologies." *Clean Technologies and Environmental Policy*, volume 4(1):pp. 32–43, July 2002.

[22] "Ultraviolet Disinfection." Wastewater Technology Fact Sheet, United States Environmental Protection Agency, September 1999.

[23] Jeyanayagam, S.S. and Bryck, J. "Practical Considerations in the Use of UV light for Drinking Water Disinfection." presented at the International Conference on Environmental Engineering in Niagara Falls, Ontario, Canada, July 2002.

[24] United States Environmental Protection Agency, Washington, DC. *Ultraviolet Disinfection Guidance Manual, Draft*, June 2003.

[25] Cabaj, Alexander. *personal communication.*

[26] Krieger, Hanno. *Grundlagen der Strahlungsphysik und des Strahlenschutzes*. B. G. Teubner Verlag, first edition, June 2004.

[27] Deutsches Institut für Normung e.V., Berlin. *DIN 5031-7: Strahlungsphysik im optischen Bereich und Lichttechnik; Benennung der Wellenlängenbereiche*, 1984.

[28] Matthes, R. "ICNIRP Guidelines: Guidelines on Limits of Exposure to Ultraviolet Radiation of Wavelengths Between 180 nm and 400 nm (Incoherent Optical Radiation)." *Health Physics*, volume 87(2):pp. 171–186, 2004.

[29] International Programme on Chemical Safety. *Environmental Health Criteria Monographs 160: Ultraviolet radiation*, 1994.

[30] Hirschmann, Georg, Cabaj, Alexander, Sommer, Regina, Mann, Martin, Windischbauer, Gerhard and Rotter, Manfred. "Biodosimetrische und strahlungsmesstechnische Untersuchung einer UV-Desinfektionsanlage für Trinkwasser mit Niederdruck Quecksilberdampfstrahler." Technical report, ÖFPZ Arsenal Ges.m.b.H., Veterinärmedizinische Universität Wien, Medizinische Universität Wien, October 2004.

[31] Hirschmann, Georg, Cabaj, Alexander, Sommer, Regina, Pascoli, Gert, Windischbauer, Gerhard and Rotter, Manfred. "Biodosimetrische und strahlungsmesstechnische Untersuchung einer UV-Desinfektionsanlage für Trinkwasser mit Niederdruck Quecksilberdampfstrahler." Technical report, ÖFPZ Arsenal Ges.m.b.H., Veterinärmedizinische Universität Wien, Medizinische Universität Wien, March 2005.

[32] Hirschmann, Georg, Cabaj, Alexander, Sommer, Regina, Pascoli, Gert, Windischbauer, Gerhard and Rotter, Manfred. "Biodosimetrische und strahlungsmesstechnische Untersuchung einer UV-Desinfektionsanlage für Trinkwasser mit Niederdruck Quecksilberdampfstrahler." Technical report, ÖFPZ Arsenal Ges.m.b.H., Veterinärmedizinische Universität Wien, Medizinische Universität Wien, March 2005.

[33] Sommer, Regina. *personal communication.*

[34] Fluent Inc., Lebanon, NH. *FLUENT 6.2 User's Guide*, January 2005.

[35] Ferziger, Joel H. and Perić, Milovan. *Computational Methods for Fluid Dynamics*. Springer-Verlag, 3., rev. ed. edition, 2002.

[36] Fluent Inc., Lebanon, NH. *GAMBIT 2.2 User's Guide*, September 2004.

[37] "NIST Chemistry WebBook - Thermophysical Properties of Fluid Systems." http://webbook.nist.gov/chemistry/fluid/, last checked March 10th, 2006.

[38] "Release on the Refractive Index of Ordinary Water Substance as a Function of Wavelength, Temperature and Pressure." Technical report, The International Association for the Properties of Water and Steam, Erlangen, Germany, 1997.

[39] Press, William H., Teukolsky, Saul A., Vetterling, William T. and Flannery, Brian P. *Numerical Recipes in C, The Art of Scientific Computing*. Press Syndicate of the University of Cambridge, 2nd edition, 1992. Available online at http://www.numrec.com/, last checked March 10th, 2006.